Robotica: (2021) volume 39, pp. 291–316. © The Author(s), 2020. Published by Cambridge University Press.
doi:10.1017/S0263574720000375

Continuous Finite-Time Torque Control for Flexible Assistance Exoskeleton with Delay Variation Input

Tao Xue†, ZiWei Wang†, Tao Zhang†∗, Ou Bai‡, Meng Zhang†¶ and Bin Han§

†*Department of Automation, Tsinghua University, Beijing 100084, China*
‡*Department of Electrical and Computer Engineering, Florida International University, Miami, FL 33174, USA*
¶*Move Robotics Technology Company, Ltd., Shanghai 201306, China*
§*School of Mechanical Science and Engineering, Huazhong University of Science and Technology, Wuhan 430074, China*

(Accepted May 3, 2020. First published online: August 13, 2020)

SUMMARY
Accurate torque control is a critical issue in the compliant human–robot interaction scenario, which is, however, challenging due to the ever-changing human intentions, input delay, and various disturbances. Even worse, the performances of existing control strategies are limited on account of the compromise between precision and stability. To this end, this paper presents a novel high-performance torque control scheme without compromise. In this scheme, a new nonlinear disturbance observer incorporated with equivalent control concept is proposed, where the faster convergence and stronger anti-noise capability can be obtained simultaneously. Meanwhile, a continuous fractional power control law is designed with an iteration method to address the matched/unmatched disturbance rejection and global finite-time convergence. Moreover, the finite-time stability proof and prescribed control performance are guaranteed using constructed Lyapunov function with adding power integrator technique. Both the simulation and experiments demonstrate enhanced control accuracy, faster convergence rate, perfect disturbance rejection capability, and stronger robustness of the proposed control scheme. Furthermore, the evaluated assistance effects present improved gait patterns and reduced muscle efforts during walking and upstair activity.

KEYWORDS: Compliant human–robot interaction; Series elastic actuator; Force control; Finite-time control; Fluctuated delay input; Robotic exoskeleton.

1. Introduction

The wearable exoskeleton is a powered anthropomorphic electromechanical system for strength enhancement, load carrying, exercise rehabilitation, and walking assistance. An increasing number of people show strong demand for the assistive robotic exoskeleton, that is, walking assistance for elderly and disabled people with weakened skeletal muscles, load carrying for the individual combat system, injury preventing for industrial workers, etc.[1,4] Various research institutes have developed different types of exoskeletons over these years, including LOwer-extremity Powered ExoSkeleton,[2] Hybrid Assistive LImb,[19] Gait Enhancing and Motivation System (GEMS),[3] Lokomat,[34] Stride Management Assist (SMA),[35] Soft ExoSuit,[14] etc. Recent research shows that the metabolic rate can be reduced by 9.3% for walking and 4.0% for running with the assistance of hip exoskeleton.[44]

∗ Corresponding author. E-mail: taozhang@tsinghua.edu.cn

https://doi.org/10.1017/S0263574720000375 Published online by Cambridge University Press

As a typical human–robot cooperation system, the exoskeleton must have direct interaction with humans, thus safety is a critical concern. Exoskeletons equipped with traditional high-stiffness actuators have to force the limb to move exactly with the predefined trajectory regardless of the human intentions. In this case, the robot is stiff to human and sometimes even move against the intentions, which will introduce critical safety concerns. On the contrary, the series elastic actuator (SEA) is able to achieve compliant control through instant force feedback via a soft elastomer installed between the actuator and human limb.[12] In this way, low impedance of actuator can be obtained to realize high interaction compliance, where the intrinsic safety of exoskeleton assistance can be guaranteed. Moreover, due to its greater shock tolerance, lower reflected inertial, direct force control, and efficient energy storage, SEA has been widely applied to various physical Human-Robot Interaction applications, especially for the force-controlled exoskeleton with natural assistance.[15,16,18,30,31]

Force control of SEA in exoskeleton system is characterized by human-in-the-loop, where the actuation system is disturbed with ever-changing human–exoskeleton interaction, model uncertainties, and delayed state sensing. Researchers have investigated several control strategies to address this issue, and the approaches can be roughly divided into Proportional-Integral-Derivative (PID)-based control,[12] observer-based control,[36–38] adaptive control,[16,39,41] $H\infty$ control,[40] and sliding mode control (SMC).[17] Pratt first proposed a PID controller with feedforward algorithm to compensate partial load dynamics,[12] where the control performance is influenced by the time-varying load dynamics since the compensation is rough and incomplete. To improve the control performance, disturbance observer was proposed to estimate and reject unknown interaction dynamics and modeling uncertainties in ref. [37]. To further enhance the robustness in the presence of uncertainties originated by variations in the human dynamics, Sehoon et al. incorporated the observer with a two-mass dynamic system to achieve high-precious model-based control, where the two-mass system is used to approximate the most of interaction dynamics while the observer is to address the remain disturbances.[38] In adaptive control scheme, Calanca suggested an online adaptive gain control scheme based on model reference adaptive control to match the changing conditions.[16] In this approach, human-adaptive force control can be seen as a pole placement where the time-varying load dynamics is estimated and canceled. An interactive learning impedance controller was developed to learn the human dynamics through a series of repetitive actions in ref. [39], and the learned features were used to optimize the control parameters online to adapt to the environment. $H\infty$ mixed-sensitivity synthesis method was developed to ensure robust performance of a variable impedance control strategy,[40] where the stability is primarily guaranteed by sacrificing control performance. Since finite-time control has two unique properties, faster convergence speed as well as better disturbance rejection performance,[10] SMC was subsequently applied into the SEA torque control system.[11,17] Meng et al. incorporated Levant's arbitrary order sliding-mode differentiator into the sliding mode torque controller, where the disturbances are suppressed via both the observer and SMC.[11] Regarding the chattering phenomenon caused by sign function, a continuous approximate sliding mode controller is developed to guarantee the practicability. In summary, the above passivity-based control including PID control and observer-based control are essentially infinity-time convergence, providing a high level of stability but some limitations, for example, the virtual inertia of controlled motor cannot be reduced beyond one half of its physical inertia, the virtual stiffness of a SEA cannot be increased over the physical spring stiffness due to the passivity limitation. More importantly, the control performance is heavily dependent on the disturbance observation accuracy, which suggests a higher requirement on observer design. In adaption control, some assumptions about the unknown disturbance have to be made, which is not general for practical complicated situations. Still worse, adaption method needs time for adjustment and it might not be applicable to fast-changing load dynamics. In SMC, high-frequency switching control signal in SMC will cause chattering phenomenon, while continuous approximation of SMC, that is, power reaching rule and boundary layer method,[8] will induce static errors.

Note that most of the aforementioned SEA control theories are focused on the precise torque control with instant input, while the fluctuation input caused by time delay is often ignored in the exoskeleton system. Regarding human intention perception, it is barely impossible to detect human intention directly; therefore, the exoskeleton usually sets the assistive torque reference based on the estimated intention with the biological sensors, that is, electromyogram (EMG),[19] electroencephalograph/electrooculography,[20] body capacitance,[21] muscle stiffness,[22] etc. or the kinematical/kinetic sensors, such as foot pressure, inertial measurement unit (IMU), joint position/velocity sensors, and

https://doi.org/10.1017/S0263574720000375 Published online by Cambridge University Press

so on. Among them, gait pattern recognition-based methods, such as adaptive oscillator, have been popular due to its less sensor requirement and strong robustness,[4,13,32,42,43] and it has been successfully applied into GEMS, SMA, etc. In this sensing framework, intention signal transfers from the brain, central nervous system (CNS), skeletal muscles to exoskeleton sensors, gait state estimation algorithm and finally reaches the torque controller. There is an inevitable time delay in this process, and it will result in an extra mismatched disturbance in system dynamical equations. Note that the extra disturbance, if not considered properly, will lead to degraded performance or even instability.[33] However, to the author's knowledge, the fluctuated time delay has not been addressed in forced control assistive exoskeleton.

To address the above challenges, especially for the interaction dynamics and fluctuated time delay, this paper first proposes a new high-performance disturbance observer incorporating the equivalent control concept to estimate the fast-changing interaction dynamics and extra time-delay disturbances. With the estimated disturbance, a continuous fractional power torque control law is then designed to achieve perfect matched/unmatched disturbance rejection and finite-time convergence. Moreover, the Lyapunov function is constructed with the iteration concept and integral adding power technique to demonstrate global finite-time convergence in theory. The main contributions of this paper are stated as follows:

- A new nonlinear sliding mode disturbance observer is designed by utilizing backstepping and equivalent control techniques to achieve faster convergence and stronger anti-noise capability simultaneously. Meanwhile, a continuous fractional power torque control law is proposed to ensure uncompromised performance, that is, perfect matched/unmatched disturbance rejection and global finite-time convergence. Moreover, the global finite-time stability is proved in theory by the constructed Lyapunov function with an integral adding power technique. Furthermore, the proposed high-performance torque control scheme can be easily extended to other applications except for exoskeletons.
- A continuous torque control scheme is developed to achieve high-performance control for the SEA force-controlled exoskeleton system, which is disturbed by ever-changing human–exoskeleton interaction, model uncertainties, and delayed input. It has several unique properties, that is, higher accuracy, faster convergence rate, perfect disturbance rejection capability, well static–dynamic performance, and stronger robustness. In this scheme, both precision and stability can be enhanced while it is just a trade-off for existing methods. Moreover, the control performance, like specific convergence time, can be designated in advance when designing this controller.
- Different from finite-time switching control, the output of the proposed torque control scheme is continuous and can be applied to the physical SEA system, which will contribute to developing safer and more compliant exoskeletons. Moreover, it does not need any prior knowledge or assumptions on the various disturbance, which expanded its applications to most force control scenarios. Besides, both the simulation and physical experiments have validated the superior performance and unique properties of torque control. Furthermore, the assistance effects by torque-controlled exoskeleton are also evaluated, and the results provide definitive evidence on the improved gait pattern, and reduced muscle activations and efforts.

2. Problem Formulation and Preliminaries

2.1. Exoskeleton platform

We have developed a flexible hip assistive exoskeleton (FHAE) to provide flexion-extension assistance on the hip as shown in Fig. 1. It is comprised of a hybrid soft rigid waist belt, a backpack with power supply, driver circuits and control modules, and two SEA connected with two links that are extended down to the thigh. The FHAE has four DOFs aligned with hip, and two active DOFs in the flexion-extension direction, while the other two passive DOFs in the adduction-abduction direction for walking agility. The SEA is driven by a flat brushless DC motor (Maxon Motor, EC45-70W) via a harmonic gear reducer. The motor has a maximum continuous torque of 0.128 Nm and a maximum speed with 6000 RPM, which results in a rating output torque 12.8 Nm and a maximum 60 RMP velocity of SEA with 100:1 reduction rate. Besides, a built-in relative encoder with 1000 lines is embedded in this actuator, and it implies 4000 counts per revolution on the motor side and 400,000

https://doi.org/10.1017/S0263574720000375 Published online by Cambridge University Press

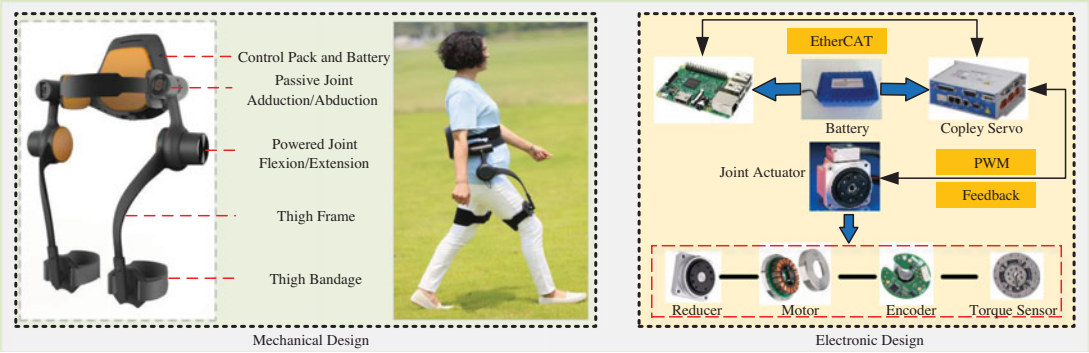


Fig. 1. Prototype of flexible hip assistive exoskeleton (FHAE) robot.

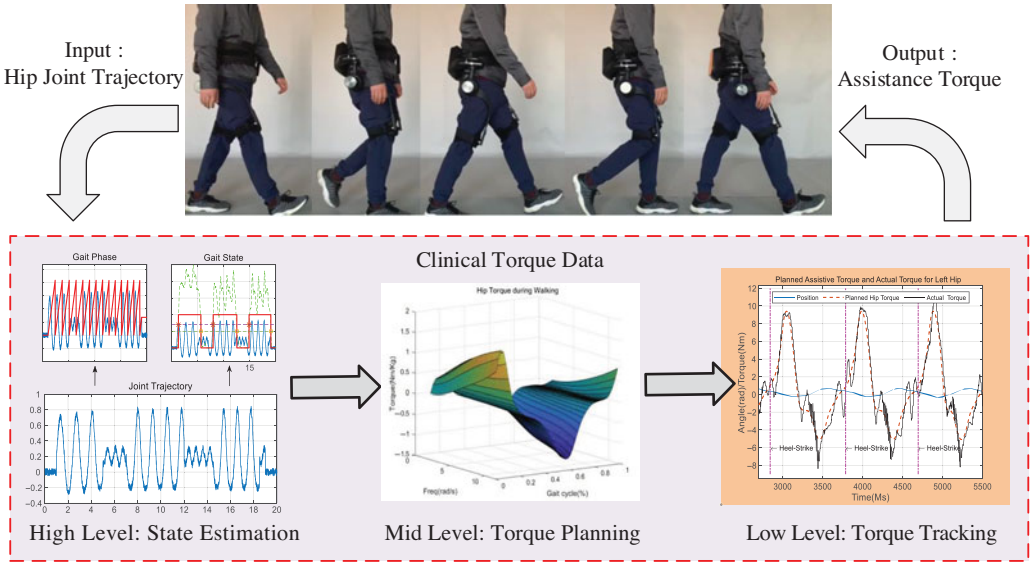


Fig. 2. Control architecture of flexible hip assistive exoskeleton (FHAE) robot.

counts per revolution on the output side. The terminal is equipped with a single-axis torque sensor (SRI M2210A) to provide instant force feedback, whose stiffness is 80 KNm/rad and the maximum capacity is 50 Nm.

The electrical system of the hip exoskeleton is responsible for high-level assistance planning, low-level motor control, sensor information acquisition, processing, and communicating. The main control unit is a Raspberry Pi 3B platform with Ubuntu MATE 16.04 OS and Robot Operating System installed. A commercial DC motor driver (Copley Accelnet Plus AE2-090-30) is used to realize three-loop control of actuators, whose update frequency is 16 KHz for the current loop. It also provides the encoder and current states to the high-level controller instantly. Besides, a high-speed EtherCAT field bus with 100 Mbps is equipped and all the slave nodes communicate with a soft EtherCAT master running in the Raspberry Pi.

The multi-level control architecture is described as shown in Fig. 2. With the measured hip joint trajectory, the high-level controller implemented an algorithm to adapt and learn the gait features such as gait length, gait frequency, gait states, and the most important gait phase. Adaptive oscillator is a common approach to sense the gait phase due to its less measurement and high robustness. These features are critical as they provide information regarding the timing and amplitude of assistance power. The mapping relationship from gait states to assistance force is established in the mid-level controller and there are several solutions such as impedance, position, sEMG, and human motion capture data-based control. In the mid-level control of FHAE, a nominal biological hip torque database with respect to walking speed and gait phase has been constructed on the basis of clinical data. It generates the assistance torque profile for both hip flexion and extension direction by mimicking

https://doi.org/10.1017/S0263574720000375 Published online by Cambridge University Press

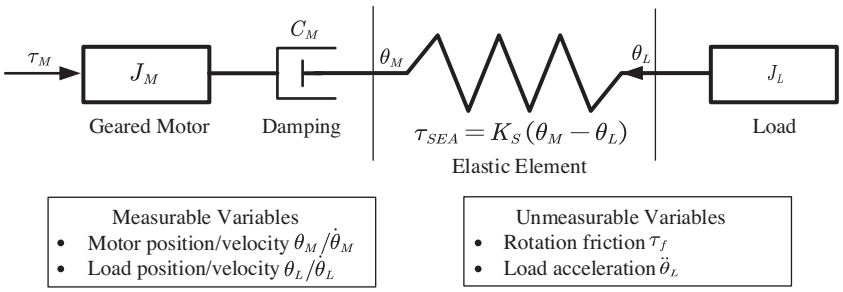


Fig. 3. Mechanical structure of series elastic actuator.

the human biological hip joint torque. The low-level controller is responsible to track the desired assistance torque profile from the output of mid-level by feedback control. The essential characteristics of the robotic exoskeleton are human-in-the-loop, where the actuation dynamics can be not only affected by the internal disturbances from the driving system but also strongly disturbed with the unpredictable ever-changing body movements. To obtain a desired torque control performance, the various disturbances suppression and rapid error convergence rate have to be well considered. The article is going to focus on the high-performance torque control of SEA.

2.2. Problem formulation

Consider the SEA system in FHAE as shown in Fig. 3, where the left component is the geared motor while the right is the human load. The elastic element is installed between the motor and load to provide instant force feedback, whose bearing torque is proportional to the deformation. The motor shows inertia and damping dynamic characteristics on account of the motor shaft and rotation friction. Note that the human dynamics are completely unknown, therefore regraded as the mass block for simplification. It is reasonable because the load dynamics are treated as a disturbance in this paper and the proposed torque controller is not dependent on the load term. In the system, motor position and velocity $\theta_M, \dot{\theta}_M$ and load position and velocity $\theta_L, \dot{\theta}_L$ can be measured via installed encoders. The rotation friction τ_f, time delay Δt, and load acceleration $\ddot{\theta}_L$ are unknown. The input of the system is controlled motor electromagnetic torque τ_M, while the applied force τ_{SEA} measured by SEA is the output. The controller aims to let the SEA output torque track prescribed reference in finite-time while maintaining the internal stability of the closed-loop system. The dynamical system is modeled as

$$\begin{cases} \dot{\Delta}\theta = \dot{\theta}_M - \dot{\theta}_L \\ \ddot{\theta}_M = J_M^{-1}\left(\tau_M - K_S\Delta\theta - C_M\dot{\theta}_M\right) - J_M^{-1}\tau_f \end{cases} \tag{1}$$

where θ_M, θ_L are the rotary angle of the motor side and load side, respectively, while $\dot{\theta}_M, \dot{\theta}_L$ are the rotary velocity. $\Delta\theta = \theta_M - \theta_L$ represents elastomer deformation and K_S stands for the stiffness coefficient of elastomer. J_M, J_L, C_M, C_L are the rotary inertia and damping coefficients for the motor side and load side, respectively. Note that friction τ_f and human dynamics cannot be obtained directly, therefore regarded as disturbances in this paper.

Ideally, the desired hip assistive force should be instant with the motion intention to realize assist as expected. However, intention transmission in the human–exoskeleton coupling system is a long process, which is from the brain, central nerve system, skeletal muscle to sensors, and multi-level assistance control. Note that in this loop, there is an inevitable fluctuated time delay consisting of inherent nerve conduction time, muscle response time, and signal processing time.[26,27] Furthermore, the electrical activity of the neuromuscular system is a process of production and transmission of neural action potential pulse, which is quite easily affected by environments, especially for elderly people.[23] With the fluctuated time delay between intentions and control systems, even a smooth trajectory intention is likely to be oscillatory when it spreads to the input of the low-level assistance torque controller. Therefore, the extra disturbance caused by the transmission delay has to be well considered.

Considering all the disturbance and time delay in FHAE, the diagram of SEA system is shown in Fig. 4. The obtained desired assistive force is contaminated with time delay Δt at the source.

https://doi.org/10.1017/S0263574720000375 Published online by Cambridge University Press

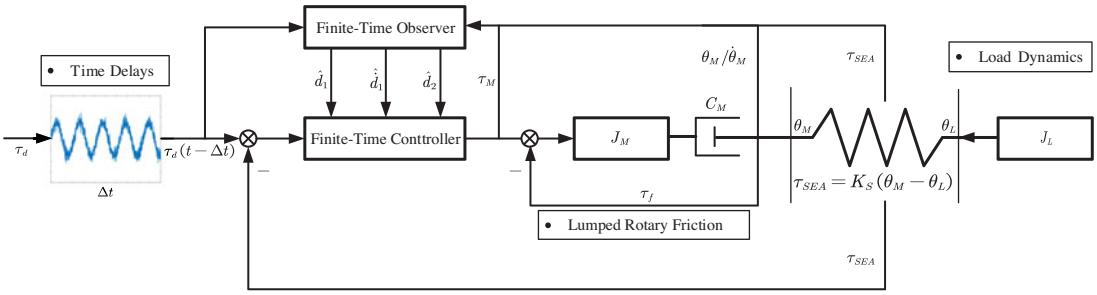


Fig. 4. Diagram of proposed SEA control scheme in FHAE.

Besides, rotation friction and load acceleration are also disturbances to the torque control system. Regarding the control scheme, a composite controller consisting of a finite-time observer and finite-time controller is designed to achieve high-performance torque control, where the observer is utilized to estimate the lumped disturbances, while the tracking performance and robustness are guaranteed by the controller.

Let $\tau_d\ (t-\Delta t)$ be the desired torque from estimated motion intention and choose the error variable $x_1 = \Delta\theta - K_S^{-1}\tau_d\ (t-\Delta t)$, $x_2 = \Delta\dot{\theta} - K_S^{-1}\dot{\tau}_d\ (t-\Delta t)$. Note that the derivate of delayed input will introduce extra terms about $\dot{\Delta}t$, as shown in Eq. (2).

$$\frac{d\tau_d\ (t-\Delta t)}{dt} = \dot{\tau}_d\ (t-\Delta t) - \dot{\tau}_d\ (t-\Delta t)\ \dot{\Delta}t. \tag{2}$$

Taking the derivate of x_1, x_2 gives

$$\begin{cases} \dot{x}_1 = \Delta\dot{\theta} - K_S^{-1}\dot{\tau}_d(t-\Delta t) + K_S^{-1}\dot{\tau}_d(t-\Delta t)\dot{\Delta}t \\ \dot{x}_2 = \Delta\ddot{\theta} - K_S^{-1}\dot{\tau}(t-\Delta t)(1-\dot{\Delta}t) \end{cases} \tag{3}$$

Substituting $\Delta\ddot{\theta} = \ddot{\theta}_M - \ddot{\theta}_L$ and Eq. (1) into the Eq. (3), then the error dynamics has the form

$$\begin{cases} \dot{x}_1 = x_2 + K_S^{-1}\dot{\tau}_d\ (t-\Delta t)\ \dot{\Delta}t \\ \dot{x}_2 = J_M^{-1}\left(\tau_M - K_S\Delta\theta - C_M\dot{\theta}_M\right) - J_M^{-1}\tau_f - \ddot{\theta}_L \\ -K_S^{-1}\ddot{\tau}_d\ (t-\Delta t) + K_S^{-1}\ddot{\tau}_d(t-\Delta t)\dot{\Delta}t \end{cases} \tag{4}$$

In this paper, the time delay, friction together with load dynamics are regarded as lumped perturbation, which is shown in Eq. (5).

$$\begin{cases} d_1 = K_S^{-1}\dot{\tau}_d\ (t-\Delta t)\ \dot{\Delta}t \\ d_2 = -J_M^{-1}\tau_f - \ddot{\theta}_L + K_S^{-1}\ddot{\tau}_d\ (t-\Delta t)\ \dot{\Delta}t \end{cases} \tag{5}$$

Let the control output $\tau_M = K_S\Delta\theta + C_M\dot{\theta}_M + J_M K_S^{-1}\ddot{\tau}_d\ (t-\Delta t) + J_M u$, where the first three terms are used to neutralize the items in Eq. (4) while u is the real control term. Substituting τ_M into the error dynamics Eq. (4), the SEA model can be simplified as a double integral system with matched/unmatched disturbances.

$$\begin{cases} \dot{x}_1 = x_2 + d_1 \\ \dot{x}_2 = u + d_2 \end{cases} \tag{6}$$

2.3. Preliminaries

Assumption 1. *The lumped disturbance and its derivate are unknown but bounded. Thus, there exist positive constants Q_i satisfying*

$$|d_1| \le Q_1,\ \left|\dot{d}_1\right| \le Q_2,\ \left|\ddot{d}_1\right| \le Q_3,\ |d_2| \le Q_4,\ \left|\dot{d}_2\right| \le Q_5 \tag{7}$$

Remark 1. Note that we assume the lumped disturbance and its derivate are bounded. It is a reasonable assumption because, for most SEA systems, the load rotary velocity/acceleration and

https://doi.org/10.1017/S0263574720000375 Published online by Cambridge University Press

friction are indeed bounded due to the physical limitation of motor power and mechanical structure. A similar assumption is also made in ref. [7] for disturbance observer design. Furthermore, these boundary assumptions are no longer required in the control law design as discussed in Section 3.

Lemma 1 (ref. [9]). *If* $0 < \ell = \ell_1/\ell_2 < 1$, *then* $\left|x^{\ell} - y^{\ell}\right| \leq 2^{1-\ell} |x - y|^{\ell}$, *where* ℓ_1, ℓ_2 *are positive odd integers.*

Lemma 2 (ref. [25]). *Let* c, d *are positive constants and* $\gamma(x, y) > 0$ *is a positive real-value function, the following inequality holds*

$$|x|^c |y|^d \leq \frac{c}{c+d}\gamma(x, y)|x|^{c+d} + \frac{d}{c+d}\gamma^{-c/d}(x, y)|y|^{c+d} \tag{8}$$

Lemma 3 (ref. [24]). *The inequality* $(|x_1| + |x_2| + \cdots + |x_n|)^p \leq |x_1|^p + |x_2|^p + \cdots + |x_n|^p$ *holds for* $x_i \in R$, $i = 1,2, \cdots, n$, *where* p *is a real number satisfying* $0 < p \leq 1$.

Lemma 4 (refs. [5,6]). *Consider the following differential system*

$$\begin{cases} \dot{\boldsymbol{x}}(t) = \boldsymbol{f}(\boldsymbol{x}, t) \\ \boldsymbol{x}(0) = \boldsymbol{x}_0 \end{cases} \tag{9}$$

and suppose there is a continuous positive-defined differentiable function $V : \boldsymbol{U}_0 \to \mathbb{R}$ *such that*

$$\dot{V}(\boldsymbol{x}) + kV^{\alpha}(\boldsymbol{x}) \leq 0, \boldsymbol{x} \in \boldsymbol{U}_0 \backslash \{\boldsymbol{0}\} \tag{10}$$

where $\alpha \in (0, 1)$, $k > 0$, *and* $\boldsymbol{U}_0 \in \mathbb{R}^n$ *is an open neighborhood of the origin. Then the system is finite-time stable, and the settling time is* $T \leq V^{1-\alpha}(0)/k(1-\alpha)$. *In particularly, if the following inequality holds*

$$\dot{V}(\boldsymbol{x}) + \beta V(\boldsymbol{x}) + kV^{\alpha}(\boldsymbol{x}) \leq 0, \boldsymbol{x} \in \boldsymbol{U}_0 \backslash \{0\} \tag{11}$$

where $\beta > 0$ *and the settling time satisfies*

$$T = \frac{1}{\beta(1-\alpha)} \ln \frac{k + \beta V^{1-\alpha}(\boldsymbol{0})}{k}. \tag{12}$$

Lemma 5 (ref. [24]). *The inequality* $|x|^{\alpha} < 1 + |x|$ *holds for* $0 < \alpha < 1$, *where* $x \in R$.

3. Control Design

To realize high-performance torque control performance in the human–exoskeleton coupling system as shown in Fig. 4, this paper proposed a robust composite finite-time control scheme consisting of a fractional power control law and a disturbance observer. A new sliding mode observer is first designed to estimate the ever-changing human dynamics, internal/external disturbances, and time-delay disturbance. With the observed disturbances, a novel continuous control law is then proposed to reject the matched/unmatched disturbance as well as realize the finite-time convergence of torque control errors.

3.1. Disturbance observer design

With the system state equation in Eq. (6), a new finite-time disturbance observer (FDOB) is designed as Eq. (13) to estimate the disturbance d_1, $\dot{d}_1$, d_2,

$$\begin{cases} \dot{\hat{x}}_1 = x_2 + \hat{d}_1 - v_1, v_1 = k_1 \mathrm{sgn}\left(\hat{x}_1 - x_1\right), \sigma \dot{w}_1 = -w_1 + v_1 \\ \dot{\hat{d}}_1 = \dot{\hat{d}}_1 - v_2, v_2 = k_2 \mathrm{sgn}(w_1) + k_3 \hat{d}_1, \sigma \dot{w}_2 = -w_2 + v_2 \\ \ddot{\hat{d}}_1 = -k_4 \mathrm{sgn}(w_2) - k_5 \dot{\hat{d}}_1 \\ \dot{\hat{x}}_2 = u + \hat{d}_2 - v_3, v_3 = k_6 \mathrm{sgn}\left(\hat{x}_2 - x_2\right), \sigma \dot{w}_3 = -w_3 + v_3 \\ \dot{\hat{d}}_2 = -k_7 \mathrm{sgn}(w_3) - k_8 \hat{d}_2. \end{cases} \tag{13}$$

where $k_i > 0$, $i = 1,2, \cdots, 8$ are the observer coefficients, and $\hat{x}_1$, $\hat{d}_1$, $\dot{\hat{d}}_1$, $\hat{x}_2$, $\hat{d}_2$ are the estimates for x_1, d_1, $\dot{d}_1$, x_2, d_2. σ is a small positive scalar representing the time constant of the low-pass filter.

https://doi.org/10.1017/S0263574720000375 Published online by Cambridge University Press

Different from linear disturbance observer (LDOB), the control terms (e.g., v_1, v_2, v_3) are nonlinear switching functions about feedback errors which will improve the convergence rate and enhance the robustness. Moreover, the equivalent control w_1, w_3 from v_1, v_3 is obtained through a low-pass filter. In this form, the control transmission to its derivate dynamics is more smooth, meanwhile, this design will reduce the chattering phenomenon. Furthermore, state feedbacks (e.g., $k_3\hat{d}_1$, $k_5\dot{\hat{d}}_1$, $k_8\hat{d}_2$) are introduced to stabilize the observer dynamics. More importantly, in this observer scheme, not only the backstepping Lyapunov stability proof is available but also the exact convergence time can be obtained.

Take the system dynamics Eq. (4) into the observer Eq. (13), then the observer error dynamics are governed by

$$\begin{cases} \dot{e}_1 = e_2 - k_1 \mathrm{sgn}\,(e_1) \\ \dot{e}_2 = e_3 - k_2 \mathrm{sgn}\,(w_1) - k_3\hat{d}_1 \\ \dot{e}_3 = -k_4 \mathrm{sgn}\,(w_2) - k_5\dot{\hat{d}}_1 - \ddot{d}_1 \\ \dot{e}_4 = e_5 - k_6 \mathrm{sgn}\,(e_4) \\ \dot{e}_5 = -k_7 \mathrm{sgn}\,(w_3) - k_8\hat{d}_2 - \dot{d}_2 \end{cases} \tag{14}$$

where $e_1 = \hat{x}_1 - x_1$, $e_2 = \hat{d}_1 - d_1$, $e_3 = \dot{\hat{d}}_1 - \dot{d}_1$, $e_4 = \hat{x}_2 - x_2$, $e_5 = \hat{d}_2 - d_2$ are the state estimation errors.

Theorem 1. *For the simplified SEA dynamics Eq. (6), design a disturbance observer as Eq. (13). Suppose the initial states satisfy*

$$|\hat{d}_1\,(0) - d_1\,(0)\,| \le \bar{e}_2,\ |\dot{\hat{d}}_1\,(0) - \dot{d}_1\,(0)\,| \le \bar{e}_3,\ |\hat{d}_2\,(0) - d_2\,(0)\,| \le \bar{e}_5, \tag{15}$$

where $\hat{d}_1(0)$, $\dot{\hat{d}}_1(0)$, $\hat{d}_2(0)$ are the observer initial states, while $d_1(0)$, $\dot{d}_1(0)$, $d_2(0)$ are the actual initial values. Select observer gains $k_i > 0$, $i = 1,2,\cdots,8$ such that

$$\begin{gathered} k_1 - \bar{e}_2 \ge \lambda_1, k_2 - k_3 Q_1 - \bar{e}_3 \ge \lambda_2,\ k_4 - k_5 Q_2 - Q_3 \ge \lambda_3 \\ k_6 - \bar{e}_5 \ge \lambda_4,\ k_7 - k_8 Q_4 - Q_5 \ge \lambda_5 \end{gathered} \tag{16}$$

$$\bar{e}_3 = \frac{k_5 Q_2 + k_4 + Q_3}{k_5},\ \bar{e}_2 = \frac{k_3 k_5 Q_1 + k_2 k_5 + k_5 Q_2 + k_4 + Q_3}{k_3 k_5},\ \bar{e}_5 = \frac{k_8 Q_4 + k_7 + Q_5}{k_8} \tag{17}$$

where $\bar{e}_2$, $\bar{e}_3$, $\bar{e}_5$ are the upper limit of observer error e_2, e_3, e_5, while λ_1, λ_2, λ_3, λ_4, λ_5 are the positive coefficients determining the convergence time of e_1, e_2, e_3, e_4, e_5. Then, the disturbance observer is finite-time stable, that is, $e_i\,(t) \equiv 0$, $i = 1,2,\cdots,5$ for $t \ge T_{ob}$ and the convergence time is as follows

$$T_{ob} = \sqrt{2}\max\left\{\left(\frac{V_0^{\frac{1}{2}}(e_3(0))}{\lambda_3} + \frac{V_1^{\frac{1}{2}}(e_2(0))}{\lambda_2} + \frac{V_2^{\frac{1}{2}}(e_1(0))}{\lambda_1}\right), \left(\frac{V_3^{\frac{1}{2}}(e_5(0))}{\lambda_5} + \frac{V_4^{\frac{1}{2}}(e_4(0))}{\lambda_4}\right)\right\} \tag{18}$$

where V_i, $i = 1, 2, \cdots, 5$ are the Lyapunov functions defined in the stability proof part.

Remark 2. Note that the observer errors e_2, e_3, e_5 will not exceed the boundaries $\bar{e}_2$, $\bar{e}_3$, $\bar{e}_5$ when the initial state variable values are properly selected, and the rough boundaries will lead to finite-time convergence for the whole observer dynamics. Moreover, since the upper bounds Q_1, Q_2, Q_4 of d_1, $\dot{d}_1$, d_2 are smaller than $\bar{e}_2$, $\bar{e}_3$, $\bar{e}_5$, the ranges of initial values $\hat{d}_1(0)$, $\dot{\hat{d}}_1(0)$, $\hat{d}_2(0)$ are quite wide and even zero initial values are also feasible.

3.2. Control law design

With the above-estimated disturbance $\hat{d}_1$, $\dot{\hat{d}}_1$, $\hat{d}_2$, a continuous high-performance torque control law is designed as Eq. (19),

$$u = -\beta_2 \xi_2^{r_3} - \hat{d}_2 - \dot{\hat{d}}_1 \tag{19}$$

https://doi.org/10.1017/S0263574720000375 Published online by Cambridge University Press

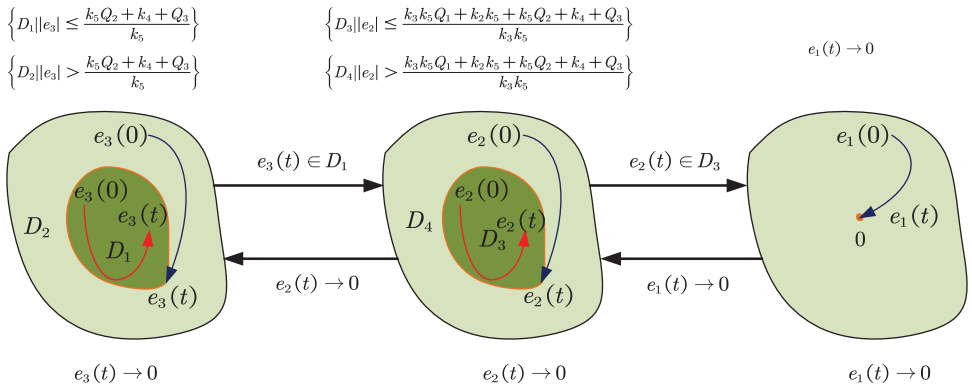


Fig. 5. Geometric representation of sets in the proof of Theorem 1.

where $\xi_2 = (\bar{x}_2)^{1/r_2} - \left(\bar{x}_2^*\right)^{1/r_2}$, $\bar{x}_2 = x_2 + d_1$, $\bar{x}_2^* = x_2^* + d_1$ and x_2^* is the virtual control law $x_2^* = -\beta_1 \xi_1^{r_2} - d_1$, $\xi_1 = x_1^{1/r_1}$. τ is a negative constant and $r_2 = r_1 + \tau$, $r_3 = r_2 + \tau$. Note that the control outputs are the fractional terms about the feedback errors, which implies the output is continuous and can be applied into physical SEA system. Besides, this virtual control design is capable to reject the matched/unmatched disturbance and more importantly guarantee global finite-time convergence.

Theorem 2. *Considering the error dynamics Eq. (6), apply the proposed composite controller as Eq. (19) and choose* $\beta_1, \beta_2, r_1, r_2, r_3, \tau$ *as follows*

$$
\begin{aligned}
&r_1 = 1,\ -1/2 < \tau < 0,\ r_2 = l_1/l_2,\ r_3 = l_3/l_4 \\
&\beta_1 \ge \beta_1^* = 2,\ \beta_2 \ge \beta_2^* \\
&\beta_2^* = c_1 + c_3 + 1,\ c_1 = \frac{r_2}{2}\left(\frac{2^{r_2-1}}{2-r_2}\right)^{(2-r_2)/r_2} \\
&c_2 = \frac{(1-\tau)(1-2\tau)}{2^{\tau+1}}\beta_1^{(r_1+r_2)/r_2}\left(\frac{2^{\tau}}{(1+\tau)(1-2\tau)\beta_1^{(r_1+r_2)/r_2}}\right)^{-(1+\tau)/(1-\tau)} \\
&c_3 = c_2 + (1-2\tau)\,2^{-2\tau}\beta_1^{1/r_2}
\end{aligned}
\tag{20}
$$

such that

$$
\tau \le \frac{2\ln\lambda}{\ln\lambda + 2\ln 2} \tag{21}
$$

where l_1, l_2, l_3, l_4 *are positive odd integers satisfying* $0 < l_1/l_2 < 1$, $0 < l_3/l_4 < 1$ *and* λ *is a positive constant determining the convergence rate of the errors. Then, the SEA system Eq. (6) is globally finite-time stable and the convergence time is as Eq. (22), where the definition of* $V_2(0)$ *is in the stability proof contents.*

$$
T_{reach} \le \frac{\tau - 2}{\lambda\tau} V_2(0)^{\frac{\tau}{\tau-2}} \tag{22}
$$

Remark 3. τ and λ are strongly correlated with the control performance, for example, convergence time and error band, therefore, should be chosen carefully with the control requirements.

4. Stability Analysis

4.1. Proof of Theorem 1

The proposed observer Eq. (13) consists of two individual sub-observers: one for the disturbance $d_1, \dot{d}_1$ estimation and the other for d_2. Here we give the proof of finite-time convergence for the first observer, while the other sub-observer can be proven in a similar method. The Lyapunov stability proof process is shown in Fig. 5, where D_1, D_2, D_3, D_4 are the predefined error regions. In this proof process, e_3 is first proven to be restricted to a fixed region D_1, followed by the e_2 limited in

https://doi.org/10.1017/S0263574720000375 Published online by Cambridge University Press

region D_3. Then the rough boundaries of D_1, D_3 are used to prove finite-time convergence of e_1. When e_1 converges to zero, the results will lead to finite-time convergence of e_2 in turn. Finally, e_3 will approach zero together with the convergence of x_1, x_2.

Choose a candidate Lyapunov function $V_0(e_3(t)) = 1/2e_3^2$, and the first derivate of V_0 along the observer error dynamics (14) is given by

$$\begin{aligned}\dot{V}_0 &= e_3(-k_4\mathrm{sgn}(w_2) - k_5\hat{\dot{d}}_1 - \ddot{d}_1)\\ &\le -k_5e_3\left(e_3 + \dot{d}_1\right) + k_4|e_3| + |e_3|\left|\ddot{d}_1\right|\\ &\le -\sqrt{2}V_0^{1/2}\left(k_5|e_3| - k_5Q_2 - k_4 - Q_3\right).\end{aligned} \tag{23}$$

Define two new sets D_1, D_2 as

$$\{D_1||e_3| \le (k_5Q_2 + k_4 + Q_3)/k_5\},\ \{D_2||e_3| > (k_5Q_2 + k_4 + Q_3)/k_5\}. \tag{24}$$

It can be concluded from the results of Eq. (23) that V_0 will decrease monotonically when $e_3 \in D_2$, which means e_3 will approach the border of region D_1 and D_2 in finite time with Lemma 4. In another case, when the initial state $e_3(0) \in D_1$, e_3 will not escape from D_1 to D_2 on account of the attraction of the boundary, which means D_1 is the region of attraction. Furthermore, when choosing the proper initial value satisfying $e_3(0) \in D_1$, it can be concluded that $|e_3(t)| \le (k_5Q_4 + k_4 + Q_5)/k_5 = \bar{e}_3$ for all $t \ge 0$.

Choose another candidate Lyapunov function $V_1(e_2(t)) = 1/2e_2^2$, and taking the first derivate of V_1 gives

$$\begin{aligned}\dot{V}_1 &= e_2(e_3 - k_2\mathrm{sgn}(w_1) - k_3\hat{d}_1)\\ &\le -k_3e_2(e_2 + d_1) + |e_2||e_3| + k_2|e_2|\\ &\le -\sqrt{2}V_1^{1/2}\left(k_3|e_2| - k_2 - k_3Q_1 - |e_3|\right)\end{aligned} \tag{25}$$

With the rough constraint of $\bar{e}_3$, define two new sets D_3, D_4 as

$$\{D_3||e_2| \le (k_3Q_1 + k_2 + \bar{e}_3)/k_3\},\ \{D_4||e_2| > (k_3Q_1 + k_2 + \bar{e}_3)/k_3\}. \tag{26}$$

Similar with the above analysis, it can be concluded that D_3 is the attraction region for $|e_2|$, which means $|e_2| \le (k_3Q_1 + k_2 + \bar{e}_3)/k_3 = \bar{e}_2$ for all $t \ge 0$ by choosing the proper initial value $\hat{d}_1(0)$ satisfying $e_2(0) \in D_3$.

Again choose a candidate Lyapunov function $V_2(e_1(t)) = 1/2e_1^2$ for the variable e_1, the first derivate of V_2 along the observer error dynamics is given by

$$\begin{aligned}\dot{V}_2 &= e_1(e_2 - k_1\mathrm{sgn}(e_1))\\ &\le -\sqrt{2}V_2^{1/2}(k_1 - |e_2|)\end{aligned} \tag{27}$$

Note that $k_1 - |e_2| \ge k_1 - \bar{e}_2$, thus there exists a positive constant such that $k_1 - |e_2| \ge \lambda_1$, $\lambda_1 > 0$ and it leads to

$$\dot{V}_2 \le -\sqrt{2}\lambda_1 V_2^{1/2} \tag{28}$$

Applying Lemma 4, it can be conducted that e_1 is finite-time stable and the convergence time $T_{ob1(0)} \le \sqrt{2}V_2^{1/2}(e_1(0))/\lambda_1$, that is, $e_1 \equiv 0$ for all $t > T_{ob1(0)}$. With the concept of equivalent control in SMC theory,[8] the equivalent control for $e_1 \equiv 0$ is $\dot{e}_1 = 0$ and it leads to

$$(k_1\mathrm{sgn}(e_1))_{eq} = e_2 = w_1,\ t > T_{ob0} \tag{29}$$

where the subscript "eq" denotes the equivalent state on the sliding surface $e_1 = \dot{e}_1 = 0$. The equivalent control describes the average effect of the high-frequency switch control, thus the equivalent control can be achieve by the low-pass filter of the high-frequency switch term $\mathrm{sgn}(e_1)$[8] as

$$\sigma\dot{w}_1 = -w_1 + k_1\mathrm{sgn}(e_1) \tag{30}$$

https://doi.org/10.1017/S0263574720000375 Published online by Cambridge University Press

where τ is a small positive scalar representing the time constant of the filter. When $t > T_{ob1(0)}$, substitute the equivalent control $w_1 = e_2$ into Eq. (25) and it leads to

$$\begin{aligned}\dot{V}_1 &= e_2(e_3 - k_2\text{sgn}\,(w_1) - k_3\hat{d}_1)\\ &= e_2\,(e_3 - k_2\text{sgn}\,(e_2) - k_3\,(e_2 + d_1))\\ &\leq -\,|e_2|\,(k_2 - \bar{e}_3 - k_3 Q_1)\end{aligned} \tag{31}$$

From Eq. (31), it can be derived that there exist positive constants k_2, k_3 such that $k_2 - \bar{e}_3 - k_3 Q_1 \geq \lambda_2$, $\lambda_2 > 0$. Thus, the Eq. (31) can be further simplified as

$$\dot{V}_1 \leq -\sqrt{2}\lambda_2 V_1^{1/2} \tag{32}$$

With Lemma 4, it can be concluded that e_2 is finite-time stable, that is, $e_2 \equiv 0$, $t > T_{ob1}$ and the convergence time is $T_{ob1(1)} = T_{ob1(0)} + \sqrt{2}V_1^{1/2}\,(e_2\,(0))\,/\lambda_2$. The equivalent control for $e_2 \equiv 0$ after $t > T_{ob1(1)}$ is $w_2 = (k_2\text{sgn}(e_1) + k_3\hat{d}_1)_{eq} = e_3$. Substituting this term into $\dot{V}_0$ leads to

$$\begin{aligned}\dot{V}_0(e_3) &= e_3(-k_4\text{sgn}\,(w_2) - k_5\hat{\dot{d}}_1 - \ddot{d}_1)\\ &= e_3(-k_4\text{sgn}(e_3) - k_5(e_3 + \dot{d}_1) - \ddot{d}_1)\\ &\leq -\,|e_3|\,(k_5\,|e_3| + k_4 - k_5 Q_2 - Q_3)\end{aligned} \tag{33}$$

Similar with the previous analysis, there exist constants k_4, k_5 such that $k_5\,|e_3| + k_4 - k_5 Q_2 - Q_3 \geq \lambda_3$, $\lambda_3 > 0$, which results in finite-time stable for e_3 with Lemma 4. The convergence time of e_1, e_2, e_3 is $T_{ob1} = T_{ob1(1)} + \sqrt{2}V_0^{1/2}\,(e_3\,(0))\,/\lambda_3$. With the similar analysis, the convergence time of e_4, e_5 is $T_{ob2} = \sqrt{2}\left(V_3^{1/2}(e_5(0))/\lambda_5,\, V_4^{1/2}(e_4(0))/\lambda_4\right)$. Thus, the total convergence time of proposed observer is

$$T_{ob} = \sqrt{2}\max\left\{\left(\frac{V_0^{\frac{1}{2}}(e_3(0))}{\lambda_3} + \frac{V_1^{\frac{1}{2}}(e_2(0))}{\lambda_2} + \frac{V_2^{\frac{1}{2}}(e_1(0))}{\lambda_1}\right), \left(\frac{V_3^{\frac{1}{2}}(e_5(0))}{\lambda_5} + \frac{V_4^{\frac{1}{2}}(e_4(0))}{\lambda_4}\right)\right\} \tag{34}$$

In summary, selecting proper observer gains and initial state values, the observer error will converge to zero in finite time, that is, $e_i = 0$, $i = 1, 2, \cdots, 5$ for all $t > T_{ob}$. Thus, the proof for Theorem 1 is completed.

4.2. Proof of Theorem 2

The stability analysis of Theorem 2 is divided into two cases: when $t < T_{ob}$, disturbance estimation is still in the transient process, and we are going to prove the errors will not escape to infinity in any time interval $[0, t]$. When all the disturbances are accurately estimated at $t > T_{ob}$, the global finite-time convergence of torque control is going to be proven. In this part, we are going to provide the proof of the latter case first and followed by the former case.

(1) Proof of Case 2

Choose Lyapunov function as follows

$$V_1 = \int_0^{x_1} \left(s^{1/r_1} - 0\right)^{2-r_2} ds \tag{35}$$

Remark 4. In order to keep the power integral type Lyapunov function positive, a positive r_1 and a negative τ should be chosen such that r_1, r_2, r_3 are ratios of two odd integers.

The first derivate of V_1 along system trajectory Eq. (6) is give by

$$\begin{aligned}\dot{V}_1 &= \xi_1^{2-r_2}\left(x_2 - x_2^* + x_2^* + d_1\right)\\ &\leq -2\xi_1^2 + \xi_1^{2-r_2}\left(x_2 - x_2^*\right)\end{aligned} \tag{36}$$

https://doi.org/10.1017/S0263574720000375 Published online by Cambridge University Press

where $\xi_1 = x_1^{1/r_1}$, x_2^* is virtual control law, here we choose $x_2^* = -\beta_1 \xi_1^{r_2} - d_1$ and $\beta_1 \geqslant \beta_1^* = 2$. Applying Lemmas 1 and 2 to scale Eq. (36), one has

$$\begin{aligned}\dot{V}_1(x_1) &\leq -2\xi_1^2 + \left|\xi_1^{2-r_2}\right| \left|(x_2 + d_1)^{\frac{1}{r_2}r_2} - \left(x_2^* + d_1\right)^{\frac{1}{r_2}r_2}\right| \\ &\leq -2\xi_1^2 + 2^{1-r_2} |\xi_1|^{2-r_2} |\xi_2|^{r_2} \\ &\leq -2|\xi_1|^2 + \frac{1}{2}|\xi_1|^2 + c_1(r_2)|\xi_2|^2\end{aligned} \tag{37}$$

where $c_1(\beta_1, r_2) = \frac{r_2}{2}\left(\frac{2^{r_2-1}}{2-r_2}\right)^{(2-r_2)/r_2}$. Choose Lyapunov function about x_1, x_2 as

$$\begin{aligned}V_2(x_1, x_2) &= V_1(x_1) + W(x_1, x_2) \\ &= \int_0^{x_1} (s^{1/r_1} - 0)^{2-r_2} ds + \int_{\bar{x}_2^*}^{\bar{x}_2} (s^{1/r_2} - \bar{x}_2^{*1/r_2})^{(2-r_2-\tau)} ds\end{aligned} \tag{38}$$

Taking first derivate of $V_2(x_1, x_2)$ along system trajectory Eq. (6) produces

$$\begin{aligned}\dot{V}_2(x_1, x_2) &= \dot{V}_1(x_1) + \frac{\partial W(x_1, x_2)}{\partial x_1}\dot{x}_1 + \frac{\partial W(x_1, x_2)}{\partial \bar{x}_2}\dot{\bar{x}}_2 \\ &\leq -2|\xi_1|^2 + \frac{1}{2}|\xi_1|^2 + c_1(r_2)|\xi_2|^2 + \left|\frac{\partial W(x_1, x_2)}{\partial x_1}\dot{x}_1\right| + \xi_2^{2-r_2-\tau}\dot{\bar{x}}_2\end{aligned} \tag{39}$$

From Lemma 1, one can obtain $\left|\int_{\bar{x}_2^*}^{\bar{x}_2} \left(s^{1/r_2} - \bar{x}_2^{*1/r_2}\right)^{2-r_2-\tau} ds\right| \leq \left|\bar{x}_2 - \bar{x}_2^*\right| \xi_2^{2-r_2-\tau}$, $\left|\bar{x}_2 - \bar{x}_2^*\right| = |\bar{x}_2^{\frac{1}{r_2}r_2} - \bar{x}_2^{*\frac{1}{r_2}r_2}| \leq |\bar{x}_2^{\frac{1}{r_2}} - \bar{x}_2^{*\frac{1}{r_2}}|^{r_2} = 2^{1-r_2}|\xi_2|^{r_2}$, and it leads to

$$\begin{aligned}\left|\frac{\partial W(x_1, x_2)}{\partial x_1}\dot{x}_1\right| &\leq \left|\bar{x}_2 - \bar{x}_2^*\right| (2 - r_2 - \tau)\, \xi_2^{2-r_2-\tau-1} \left|\frac{d\bar{x}_2^{*1/r_2}}{dx_1}\dot{x}_1\right| \\ &\leq (2 - r_2 - \tau)\, 2^{1-r_2} \xi_2^{1-\tau} \left|\frac{d\bar{x}_2^{*1/r_2}}{dx_1}\dot{x}_1\right|\end{aligned} \tag{40}$$

Applying Lemma 1 again gives

$$\begin{aligned}\left|\frac{d\bar{x}_2^{*1/r_2}}{dx_1}\dot{x}_1\right| &\leq \left|\frac{d\bar{x}_2^{*1/r_2}}{dx_1}\right| |\dot{x}_1| \\ &\leq \beta_1^{1/r_2}\frac{1}{r_1}\left|2^{1-r_2}|\xi_2|^{r_2} + \beta_1|\xi_1|^{r_2}\right|\end{aligned} \tag{41}$$

Applying Lemma 2 to scale the power product term to power additive term, one has

$$\begin{aligned}\left|\frac{\partial W}{\partial x_1}\dot{x}_1\right| &\leq (2 - r_2 - \tau)\, 2^{1-r_2}\beta_1^{1/r_2}\frac{1}{r_1}|\xi_2|^{1-\tau}\left|2^{1-r_2}|\xi_2|^{r_2} + \beta_1|\xi_1|^{r_2}\right| \\ &\leq (1 - 2\tau)\, 2^{-\tau}\beta_1^{1/r_2}|\xi_2|^{1-\tau}\left(2^{1-r_2}|\xi_2|^{1+\tau} + \beta_1|\xi_1|^{1+\tau}\right) \\ &\leq \frac{1}{2}|\xi_1|^2 + c_3(\beta_1)|\xi_2|^2\end{aligned} \tag{42}$$

$$c_3(\beta_1) = c_2(\beta_1) + (1 - 2\tau)\, 2^{-2\tau}\beta_1^{1/r_2}$$

$$c_2(\beta_1) = \frac{(1-\tau)(1-2\tau)}{2^{\tau+1}}\beta_1^{(r_1+r_2)/r_2}\left(\frac{2^\tau}{(1+\tau)(1-2\tau)\beta_1^{(r_1+r_2)/(r_2)}}\right)^{-(1+\tau)/(1-\tau)}$$

https://doi.org/10.1017/S0263574720000375 Published online by Cambridge University Press

Substituting control law Eq. (19) and inequalities Eqs. (40), (41), (42) into Eq. (39) gives

$$\begin{aligned}\dot{V}_2(x_1, x_2) &= \dot{V}_1(x_1) + \dot{W}(x_1, x_2) \\ &\leq -|\xi_1|^2 + (c_1(r_2) + c_3(\beta_1))|\xi_2|^2 - \beta_2|\xi_2|^2\end{aligned} \tag{43}$$

where $\beta_2 > \beta_2^*, \beta_2^* = c_1 + c_3(\beta_1) + 1$ and it can be conducted that

$$\dot{V}_2 \leq -\left(|\xi_1|^2 + |\xi_2|^2\right) \tag{44}$$

Meanwhile, by scaling the Lyapunov function $V_2(x_1, x_2)$, we can get

$$\begin{aligned}V_2(x_1, x_2) &= \int_0^{x_1} \left(s^{1/r_1} - 0\right)^{2-r_2} ds + \int_{\bar{x}_2^*}^{\bar{x}_2} \left(s^{1/r_2} - \bar{x}_2^{*1/r_2}\right)^{2-r_2-\tau} ds \\ &\leq |x_1| \left|s^{1/r_1} - 0\right|^{2-r_2} + \left|\bar{x}_2 - \bar{x}_2^*\right| \left|\bar{x}_2^{1/r_2} - \bar{x}_2^{*1/r_2}\right|^{2-r_2-\tau} \\ &\leq 2^{-\tau}\left(|\xi_1|^{2-\tau} + |\xi_2|^{2-\tau}\right)\end{aligned} \tag{45}$$

Applying Lemma 3, one has

$$\begin{aligned}V_2^{\frac{2}{2-\tau}}(x_1, x_2) &\leq 2^{\frac{-2\tau}{2-\tau}} \left||\xi_1|^{2-\tau} + |\xi_2|^{2-\tau}\right|^{\frac{2}{2-\tau}} \\ &\leq 2^{\frac{-2\tau}{2-\tau}}\left(|\xi_1|^2 + |\xi_2|^2\right)\end{aligned} \tag{46}$$

Establish the connection between V_2 and $\dot{V}_2$ and it leads to

$$\begin{aligned}\dot{V}_2 + \lambda V_2^{\frac{2}{2-\tau}} &\leq -\left(|\xi_1|^2 + |\xi_2|^2\right) + \lambda 2^{\frac{-2\tau}{2-\tau}}\left(|\xi_1|^2 + |\xi_2|^2\right) \\ &\leq -\left(1 - \lambda 2^{\frac{-2\tau}{2-\tau}}\right)\left(|\xi_1|^2 + |\xi_2|^2\right)\end{aligned} \tag{47}$$

where λ is the coefficient determining the finite convergence time. From Lemma 4 and Eq. (47), it can be conducted that the following inequality Eq. (48) should be satisfied to ensure finite-time convergence of error variables.

$$\tau \leq \frac{2\ln\lambda}{\ln\lambda + 2\ln 2} \tag{48}$$

Convergence time is as follows:

$$T_{reach} \leq \frac{\tau - 2}{\lambda\tau} V_2(0)^{\frac{\tau}{\tau-2}} \tag{49}$$

(2) Proof of Case 1

When $t < T_{ob}$, observer errors are not zero, which will introduce extra disturbance to the system dynamics. Here we will give the proof that the state variables are bounded and will not escape to the infinity in any $t \in [0, T_{ob}]$. Choose the candidate Lyapunov function as

$$B(x_1, x_2, \hat{d}_1) = \frac{1}{2}(x_1^2 + x_2^2 + \hat{d}_1^2) \tag{50}$$

Take the first derivate of the Lyapunov function and substitute the control law Eq. (19) into Eq. (50). Apply Lemmas 3 and 5 and it yields

$$\begin{aligned}\dot{B} &= x_1\left(x_1 + \hat{d}_1 - e_2\right) + x_2\left(u + \hat{d}_2 - e_5\right) + \hat{d}_1\left(\dot{\hat{d}}_1 - k_2\mathrm{sgn}(w_1) - k_3\hat{d}_1\right) \\ &\leq |x_1|^2 + |x_1||\hat{d}_1| + |x_1||e_2| + \beta_2|x_2|\left(1 + |x_2| + |\hat{d}_1| + \beta_1^{r_3/r_2}(1 + |x_1|)\right) \\ &\quad + |x_2||\dot{\hat{d}}_1| + |x_2||e_5| + |\hat{d}_1||\dot{\hat{d}}_1| + \frac{k_2^2}{4k_3}\end{aligned} \tag{51}$$

https://doi.org/10.1017/S0263574720000375 Published online by Cambridge University Press

Note that the observer error e_3 has been proven to be bounded with $\bar{e}_3$, and it leads to

$$|\hat{\dot{d}}_1| = |e_3 + \dot{d}_1| \leq |e_3| + |\dot{d}_1| \leq Q_4 + \bar{e}_3 = \bar{\hat{\dot{d}}}_1 \tag{52}$$

Substitute the boundary into Eq. (51), and it can be conducted that

$$\begin{aligned}
\dot{B} &\leq |x_1|^2 + \beta_2 |x_2|^2 + \frac{|x_1|^2 + |\hat{d}_1|^2}{2} + \frac{|x_1|^2 + |e_2|^2}{2} + (\beta_2 + \beta_1^{r_3/r_2}\beta_2 + |\hat{\dot{d}}_1|)\,|x_2| \\
&\quad + \beta_2 \frac{|x_2|^2 + |\hat{d}_1|^2}{2} + \beta_1^{r_3/r_2}\beta_2 \frac{|x_1|^2 + |x_2|^2}{2} + \frac{|x_2|^2 + |e_5|^2}{2} + \frac{|\hat{d}_1| + |\hat{\dot{d}}_1|^2}{2} + \frac{k_2^2}{4k_3} \\
&\leq \left(2 + \frac{\beta_1^{r_3/r_2}\beta_2}{2}\right)|x_1|^2 + \left(\frac{3}{2}\beta_2 + \frac{\beta_1^{r_3/r_2}\beta_2}{2} + \frac{1}{2} + \frac{|\beta_2 + \beta_1^{r_3/r_2}\beta_2 + \bar{\hat{\dot{d}}}_1|^2}{2}\right)|x_2|^2 \\
&\quad + \left(\frac{1+\beta_2}{2}\right)|d_1|^2 + \frac{1}{2}|e_2|^2 + \frac{1}{2}|e_5|^2 + \frac{\bar{\hat{\dot{d}}}_1^2}{2} + \frac{k_2^2}{4k_3} \\
&\leq KB + L
\end{aligned} \tag{53}$$

$$\begin{aligned}
K &= \max\left[2 + \frac{1}{2}\left(\beta_1^{\frac{r_3}{r_2}}\beta_2\right), \frac{3}{2}\beta_2 + \frac{1}{2}\beta_1^{\frac{r_3}{r_2}}\beta_2 + \frac{1}{2} + \frac{1}{2}|\beta_2 + \beta_1^{\frac{r_3}{r_2}}\beta_2 + |\hat{\dot{d}}_1||^2, \frac{1}{2}(1+\beta_2)\right] \\
L &= \frac{1}{2}|e_2|^2 + \frac{1}{2}|e_5|^2 + \frac{|\hat{\dot{d}}_1|^2}{2} + \frac{k_2^2}{4k_3}
\end{aligned} \tag{54}$$

where K and L are constants as Eq. (54). Solving the above inequality, we can obtain

$$B(x_1, x_2, d_1) \leq (B(0) - L/K)e^{Kt} + L/K \tag{55}$$

Hence, it has been proven that the system state x_1, x_2 are still bounded even in the transient process of disturbance observation. In the steady state of the observer, the finite-time convergence of the whole system has been validated in the above content. Therefore, the stability proof of the proposed torque control scheme is completed.

5. Simulation and Experiments

In this section, simulation results are first presented to evaluate the performance of the proposed torque controller. Then, the control scheme is implemented into the physical SEA testing platform to validate the robustness and practical effectiveness. Moreover, we have also applied this algorithm in human walking and squatting experiments with the assistance of the robotic exoskeleton to conclude the superiority and application limitations. We further recruited six human subjects to evaluate the assistance effects during walking and upstair activity by the assistive torque, where the impacts on spatiotemporal parameters of gait and related muscle efforts are demonstrated.

5.1. Simulation

As mentioned above, the series elastic actuation system is suffered from internal driving system disturbance, external human–exoskeleton interaction uncertainties as well as fluctuated input delay. To approximate the practical environment, we built a SEA model considering various uncertainties in MATLAB Simulink, whose nominal dynamical state equation is described in Eq. (1). The simulation parameters are set in Table I, where J_M, C_M denote the inertia and damping coefficients of actuation system, while K_S is the stiffness of elastomer. T_S, T_D represent the static and dynamical coefficients for the friction model described in Eq. (57). m_L is the human–exoskeleton interaction disturbance amplitude defined in Eq. (58). Regrading the control parameter, $k_1, \cdots, k_8$ are the feedback gains of proposed disturbance observer, while l_1, l_2, l_3 stand for the gains for linear observer in Eq. (59). $\beta_1, \beta_2, r_1, \tau, \sigma$ are the parameters of proposed torque controller, which have been defined and discussed in Section 3. In this part, the desired torque generation and simulated disturbance consisting of input delay, internal friction, and interaction uncertainties are first discussed. Then is the observer performance comparison and followed by the ultimate torque control conclusion.

https://doi.org/10.1017/S0263574720000375 Published online by Cambridge University Press

Table I. The simulation and control parameters

System parameters	Value	Control parameters	Value
J_M	$0.215\,\mathrm{Kg}\cdot\mathrm{m}^2$	$k_1, k_2, \cdots, k_8$	0.6,1.0,0.4,13.0,0.4,20,600,0.1
C_M	$1.0\,\mathrm{Nm}/(\mathrm{rad}\cdot\mathrm{s}^{-1})$	l_1, l_2, l_3	5 50 75
K_S	$100\,\mathrm{Nm}\cdot\mathrm{rad}^{-1}$	β_1, β_2	50,150
T_S	2.0 Nm	r_1	1
T_d	1.4 Nm	τ	$-2/9$
m_L	-0.1	σ	0.001

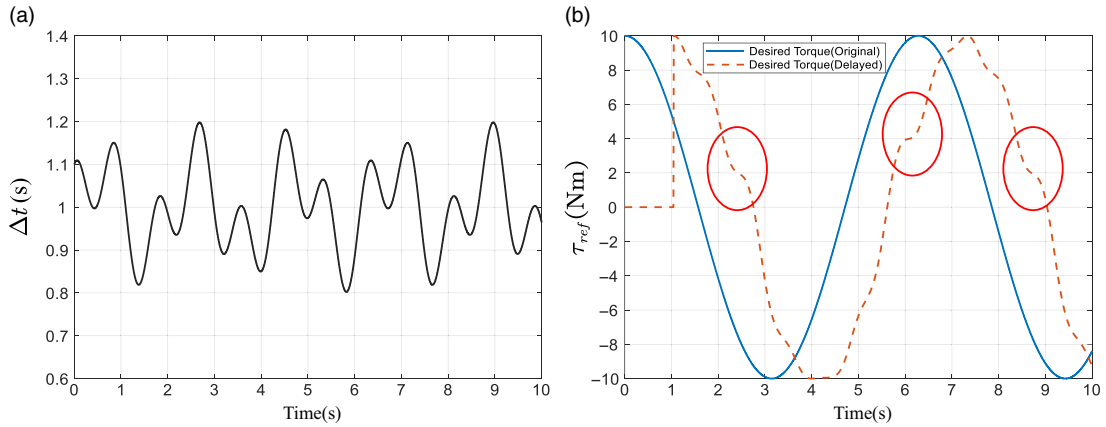


Fig. 6. Simulated time delay and delayed input torque profile.

As analyzed in Section 2, the input time delay consists of inherent nerve conduction time, muscle response time, and processing time, which is fluctuated around a constant value. Accordingly, it can be approximated with a constant value plus two sinusoids as described in Eq. (56).

$$\Delta t = 1.0 + 0.1\sin(3t) + 0.1\sin(7t) \tag{56}$$

The friction is simulated with "coulomb+viscous+stribeck" model in ref. [28] as

$$\tau_f(\dot{\theta}_M) = (T_S + (2.3 - T_S)e^{-|\dot{\theta}_M/0.15|} + T_D\dot{\theta}_M)\mathrm{sgn}(\dot{\theta}_M) \tag{57}$$

where θ_M denotes the rotation angular velocity. Since human walking is a quasi-periodic process, the human–exoskeleton interaction dynamics $\ddot{\theta}_L$ is approximated with

$$\ddot{\theta}_L = m_L\cos(t) \tag{58}$$

The original desired torque profile is assumed to be a smooth sinusoidal curve in this article, and it is transmitted to the input through a time-delay block as shown in Eq. (56). The simulated input time delay, original desired torque profile, and delayed signal are plotted in Fig. 6. It can be seen that the time delay is oscillating around a constant in a mixed higher–lower frequency, which is compatible with actual human–exoskeleton transmission delays. From Fig. 6(b), the delayed input is more fluctuated than the original, especially inside the red circles, which introduces extra disturbances on the torque control. Note that there is no input signal for the first 1 s on account of the time delay and the delayed signal is assumed to be zero at this time.

Regarding the disturbance observer, the comparison results between the proposed FDOB and LDOB are presented to highlight the superiority of FDOB. The mathematical form of LDOB[29] is given by

$$\begin{cases} \dot{\hat{z}}_1 = -l_1\hat{z}_1 + l_1(-l_1x_1 - x_2),\ \hat{d}_1 = \hat{z}_1 + l_1x_1 \\ \dot{\hat{z}}_2 = -l_2^2\hat{d}_1,\ \dot{\hat{d}}_1 = \hat{z}_2 + l_2\hat{d}_1 \\ \dot{\hat{z}}_3 = -l_3\hat{z}_3 + l_3(-l_3x_2 - u),\ \hat{d}_2 = \hat{z}_3 + l_3x_2 \end{cases} \tag{59}$$

https://doi.org/10.1017/S0263574720000375 Published online by Cambridge University Press

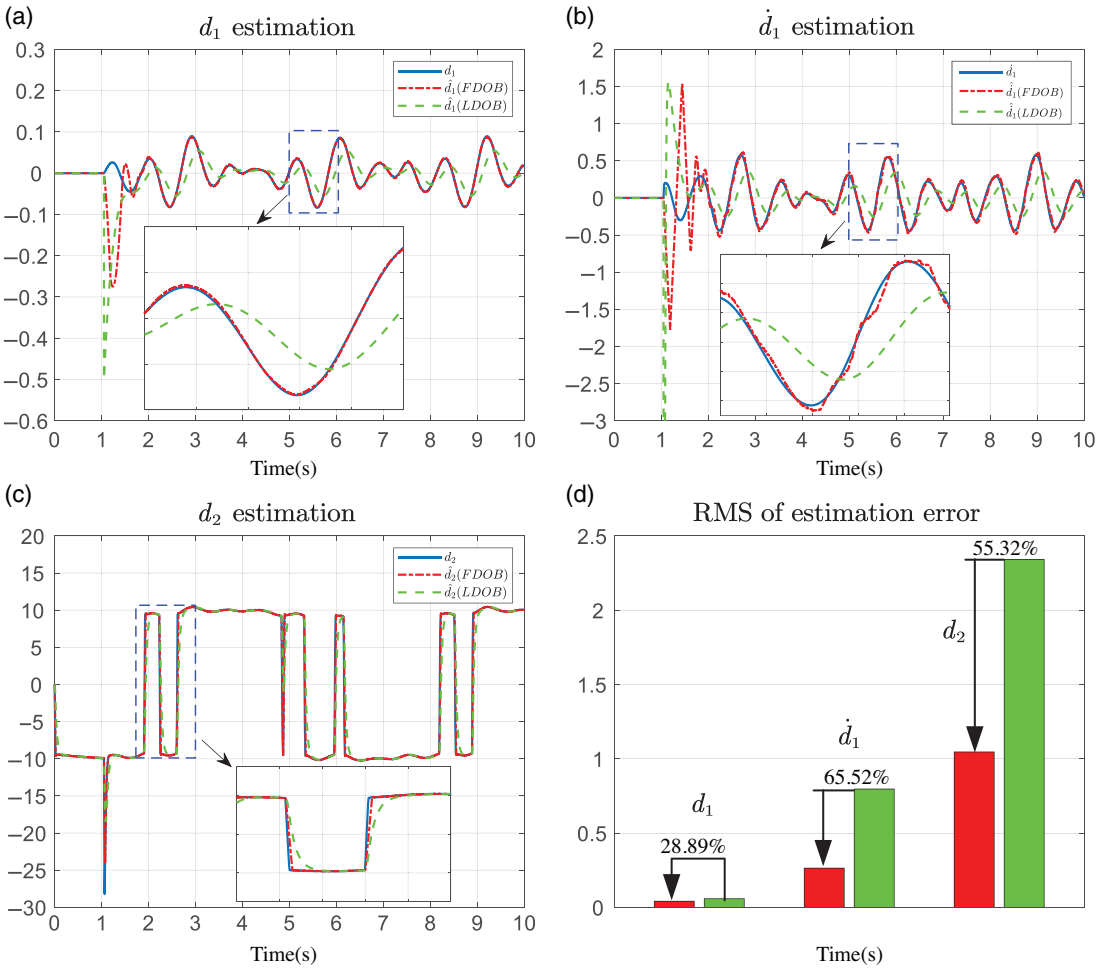


Fig. 7. Disturbance observation performance with proposed FDOB and LDOB.

where l_1, l_2, l_3 are the feedback gains defined in Table I. The estimated trajectories and quantitative results of LDOB and proposed FDOB are shown in Fig. 7.

From Fig. 7(a), both the FDOB and LDOB have estimation errors in the beginning but the overshoot of FDOB is just about half of that in LDOB. It can be seen from the enlarged figure that there exists a phase lag and amplitude error with LDOB methods, while the FDOB can achieve much better estimation accuracy. Figure 7(b) also demonstrates similar properties, such as lower overshoot, smaller phase lag, and better accuracy. Note that d_2 has some mutation points, where the signal jumps from one value to another in a very short time. From the enlarged figure in Fig. 7(c), the convergence time of FDOB is much shorter than LDOB, which further implies the faster convergence rate of finite-time control. Figure 7(d) is the RMS estimation error bars of two approaches, and it can be obtained that the disturbance estimation errors are significantly reduced and the maximum reduction is up to 65.52%. All these results provide strong evidence that the proposed FDOB behaves a much better disturbance estimation performance, such as faster convergence rate, lower overshoot, smaller phase lag, and most importantly higher accuracy.

Based on the observed disturbance, the torque tracking performances of the proposed continuous finite-time control scheme (CFTC) and traditional PID controller are illustrated, respectively in Fig. 8. To compare the control accuracy, the trajectories of torque error, its derivates, and corresponding error bars are also plotted. Figure 8(a) depicts the torque tracking trajectories, and it can be obtained that the torque trajectory under PID shows large overshoot in the beginning, while the control torque of CFTC is capable of following the input in a very short time with lower errors. Moreover, CFTC has a better control accuracy against the disturbances due to the time-delay suppression mechanism, especially in the area of the enlarged figure. Figure 8(b) presents the torque error trajectories,

https://doi.org/10.1017/S0263574720000375 Published online by Cambridge University Press

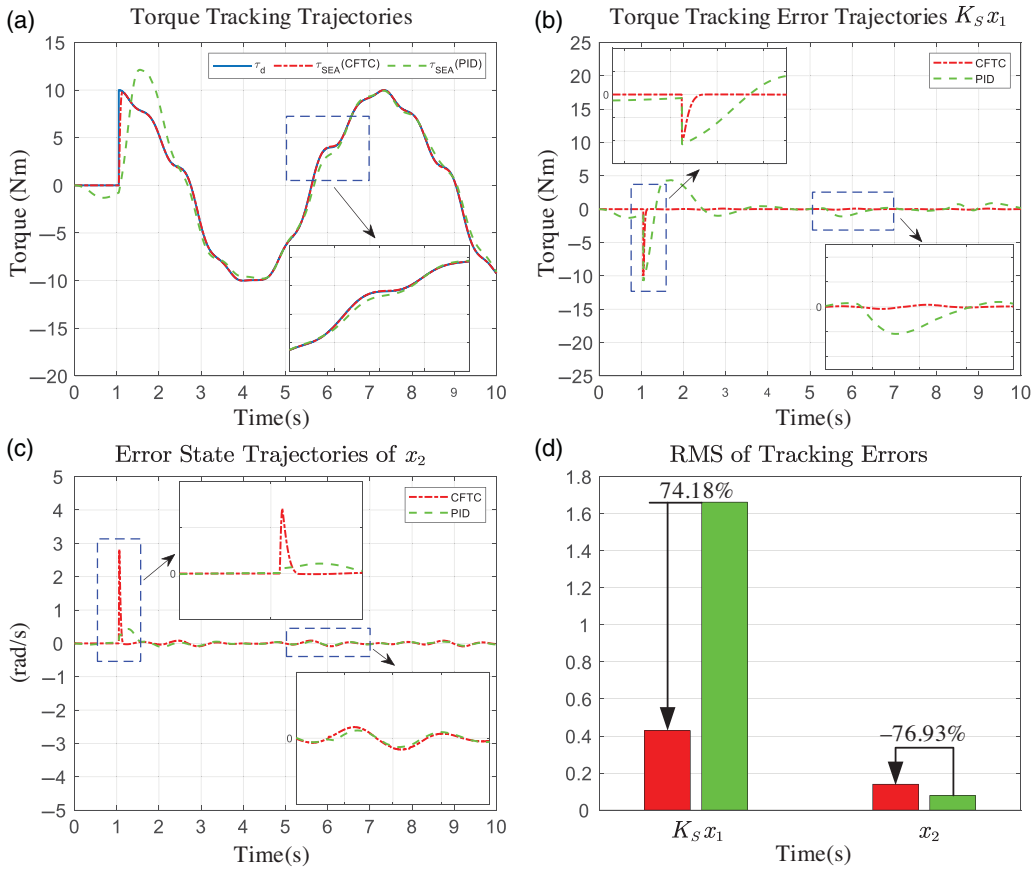


Fig. 8. Torque tracking performance with proposed CFTC controller and PID.

which also implies a faster convergence rate and higher accuracy of CFTC. Figure 8(c) is the derivate of torque error trajectories, where CFTC has a faster convergence rate but higher overshoot while PID gets a lower convergence rate but much lower overshoot. Besides, there is no significant difference in this variable under the two cases. From Fig. 8(d), the RMS of torque tracking error of CFTC is effectively reduced by 74.18% but the RMS of the derivate of torque error is increased by 76.93%. Note that x_2 in CFTC and PID cases are both kept at a relatively low level, thus the increased value have little impacts on the control performance. Moreover, the torque tracking error is all we need to focus on and the derivate is just an auxiliary variable. All the evidence demonstrates that proposed CFTC behaves superior performance than PID, such as faster convergence rate, higher control accuracy, lower overshoot, and most importantly better disturbance rejection properties, especially for the delay input.

The above simulation experiments have validated the unique properties of CFTC and the results perform as expected. However, the dynamical system is continuous and the model is relatively accurate in the simulation environment, which is, however, not possible in the physical platform. Thus, it has to be tested further with actual experiments to validate the robustness and properties of the proposed scheme.

5.2. Experiments on testing platform

We have developed a robot joint testing platform as shown in Fig. 9 to evaluate the control performance. To ensure the safety, the CFTC and PID control algorithms with FDOB are implemented in the testing platform first and then migrated to the robotic exoskeleton. The SEA testing platform is comprised of an SEA system and a human–exoskeleton interaction simulation system. The interaction dynamics are approximated with a simulated load, which is a current-controlled direct drive motor (KOLLMORGEN, CARTRIDGE DDR, C063). The SEA is actuated by HARMONIC integrated robot drive system (FHA-14C-12S17BE) with a built-in harmonic gear reducer, an absolute

https://doi.org/10.1017/S0263574720000375 Published online by Cambridge University Press

Table II. The parameters of torque control performance

Methods	**RMSE (Nm)**	**CT (s)**	**MSSE (Nm)**
CFTC	0.2383	1.036	0.2773
PID($k_\alpha = 10$)	0.4633	1.127	1.2494
PID($k_\alpha = 8$)	0.9533	1.322	2.3735
PID($k_\alpha = 6$)	1.7038	2.028	3.2360

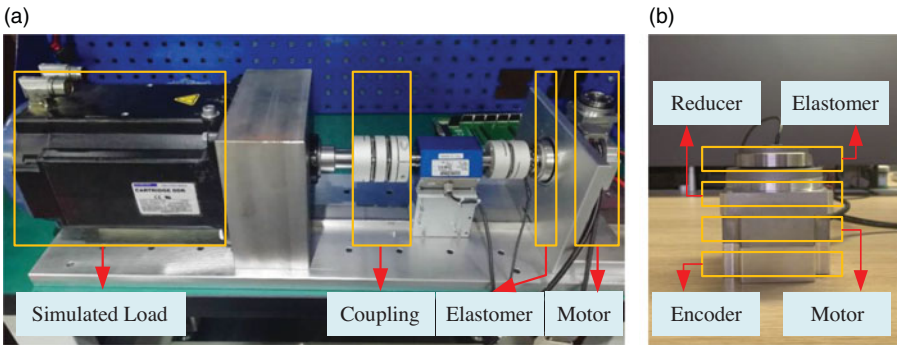


Fig. 9. Robot joint testing platform and SEA system. (a) Joint testing platform. (b) Series elastic actuator.

encoder, and a terminal torque sensor (SRI M2210). The encoder is mounted to the shaft of the motor side and it has a 16-bit multi-turn counter and a 17-bit single-turn counter, which yields a resolution of 131,072 counts/rev on the motor side. Besides, a Copley Accelnet Plus Amplifier Module (AE2-090-30) is utilized to drive the actuator, and it has three-loop control modes with the 16 KHz inner current loop. The main control unit (Raspberry Pi 3B) executes the control algorithm and communicates with the slave motor driver via a 1 KHz real-time EtherCAT field bus to update the control command and state variables.

The simulated human–exoskeleton interaction dynamics are set as Eq. (58), and the internal friction and damping disturbance are already included in the physical system. We use the same delayed torque input profile as Fig. 6 and both the proposed CFTC control scheme and PID are implemented into this system to compare the control performance. We selected three control gains for the PID algorithm, where the gains are the trade-off of control accuracy and disturbance rejection capabilities. Three indicators are chosen to evaluate the performance, where the CT is defined with the first time to enter the defined error bound 1 Nm, while maximum steady-state error (MSSE) stands for the maximum control error in steady state. The results are presented in Fig. 10 and Table II.

In Fig. 10(a), it can be obtained that higher gains result in faster convergence speed and smaller control errors in the PID scheme. However, the chattering phenomenon or even instability is likely to occur when keeping increasing the gains. From the enlarged figure, we can see that small oscillations have already occurred in the PID($K_\alpha = 10$) case, especially at the peaks and troughs. Compared with the maximum allowable gain selection in PID, the propose CFTC still presents more superior tracking capabilities with faster convergence rate, smaller errors, and most importantly no oscillations. Figure 10(b) shows the error trajectories, similar to the above analysis, CFTC has the shortest convergence time and the lowest steady-state error. Moreover, the errors have no oscillations but floating slightly around the zero from the enlarged figure. The quantitative results can be found in Fig. 10(c) and Table II. The MSSE is mostly reduced by 91.43% and RMSE is decreased by 86.01%, which implies the control accuracy has been significantly improved by CFTC. And the shorter CT also demonstrates faster convergence rate of CFTC. The results provide strong evidence that the control accuracy, convergence rate, and robustness are all enhanced by the proposed CFTC.

5.3. Experiments on hip assistance exoskeleton

The proposed CFTC torque control scheme has been further implemented into the hip assistance exoskeleton in walking and squatting assistance experiments to demonstrate the practicability. As discussed in the previous Fig. 2, the assistance torque profile is generated from the constructed nominal biological database in mid-level controller with the gait sensing input from high-level control.

https://doi.org/10.1017/S0263574720000375 Published online by Cambridge University Press

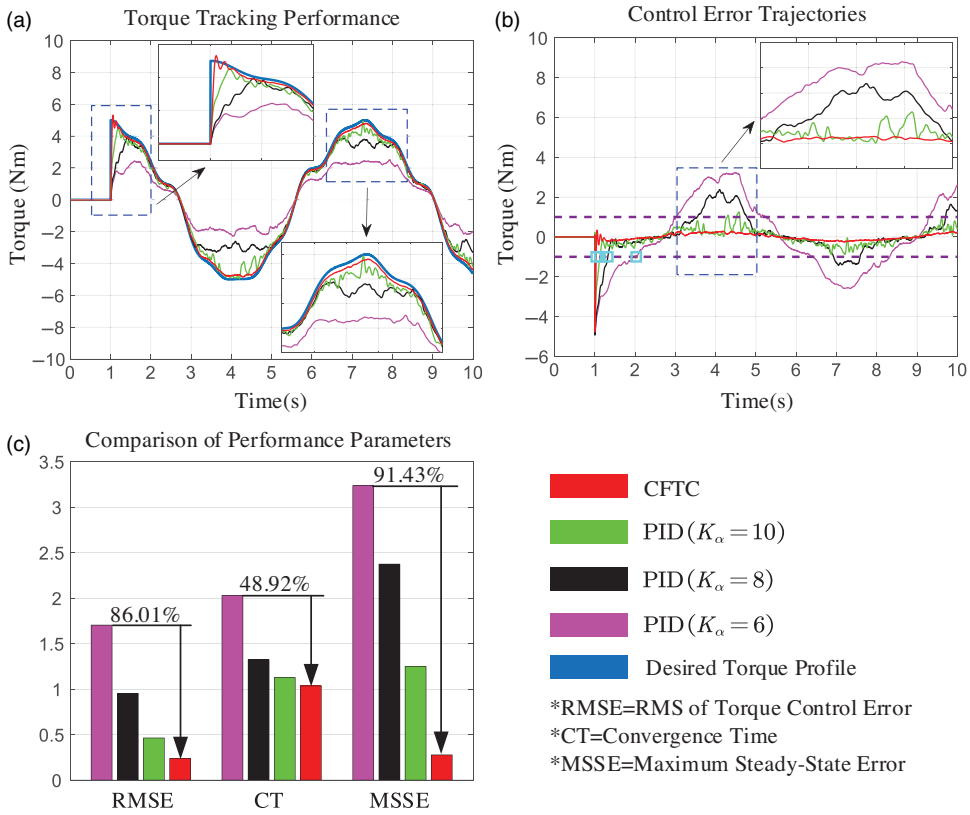


Fig. 10. Torque control performance of CFTC and PID.

And all the disturbances are included in this human–exoskeleton coupling system. Meanwhile, to make the results more convincing, several activities of daily life, including normal walking and sit-to-stand (STS), are considered. In these cases, walking motion is more dynamic while squatting is more static and these two scenarios are utilized to demonstrate the static–dynamic performance of torque control. The experimental scenes are shown in Fig. 11.

The control performance results are presented in Fig. 12, and the black dot line denotes the recognized walking states, where walking is marked with number 4 while standing and squatting are marked with number −4. From the walking results in Fig. 12(a), the desired assistance torque profile is quasi-sinusoid but slightly fluctuated on account of delayed gait state sensing, especially at the peaks and troughs. It can be obtained that the actual assistance torque is capable of tracking the desired assistance torque in the fast convergence rate and good accuracy even in the positive–negative alternating walking assistance scene. Moreover, at the walking state-changing points, the controlled torque can response to the abrupt desired signal instantly with low overshoot. In the more static squatting activities of Fig. 12(b), CFTC can also achieve pretty well control accuracy with fast response speed. Below Fig. 12(c) and (d) shows the control error trajectories of walking and squatting, respectively. It can be seen that the signals are noisier in dynamical walking than static standing or squatting, and that is because human–exoskeleton interaction disturbance is more severe during dynamical walking. And in that case, the finite-time torque control scheme has to reshape the output frequently by adaptive disturbance estimation and suppression. Fortunately, the errors are all limited within the bounds both in the static and dynamical movements. Different from simulations, there still exist torque control errors in the steady process, and that might be the result of discrete sampling date and modeling uncertainties. The RMS of torque error in walking is 0.34 Nm, while 0.28 Nm in squatting and this amplitude control errors are acceptable for human–exoskeleton interaction scenes.

In summary, both the simulation and physical experiments validate the unique properties of proposed CFTC, that is, high accuracy, fast convergence rate, perfect disturbance rejection capability, well static–dynamic performance, and strong robustness. Compared with traditional PID control, the interaction disturbance suppression capability, control stability, and accuracy are strongly enhanced,

https://doi.org/10.1017/S0263574720000375 Published online by Cambridge University Press



Fig. 11. Walking and squatting experiments with exoskeleton assistance. (a) Assistance walking experiments. (b) Assistance squatting experiments.

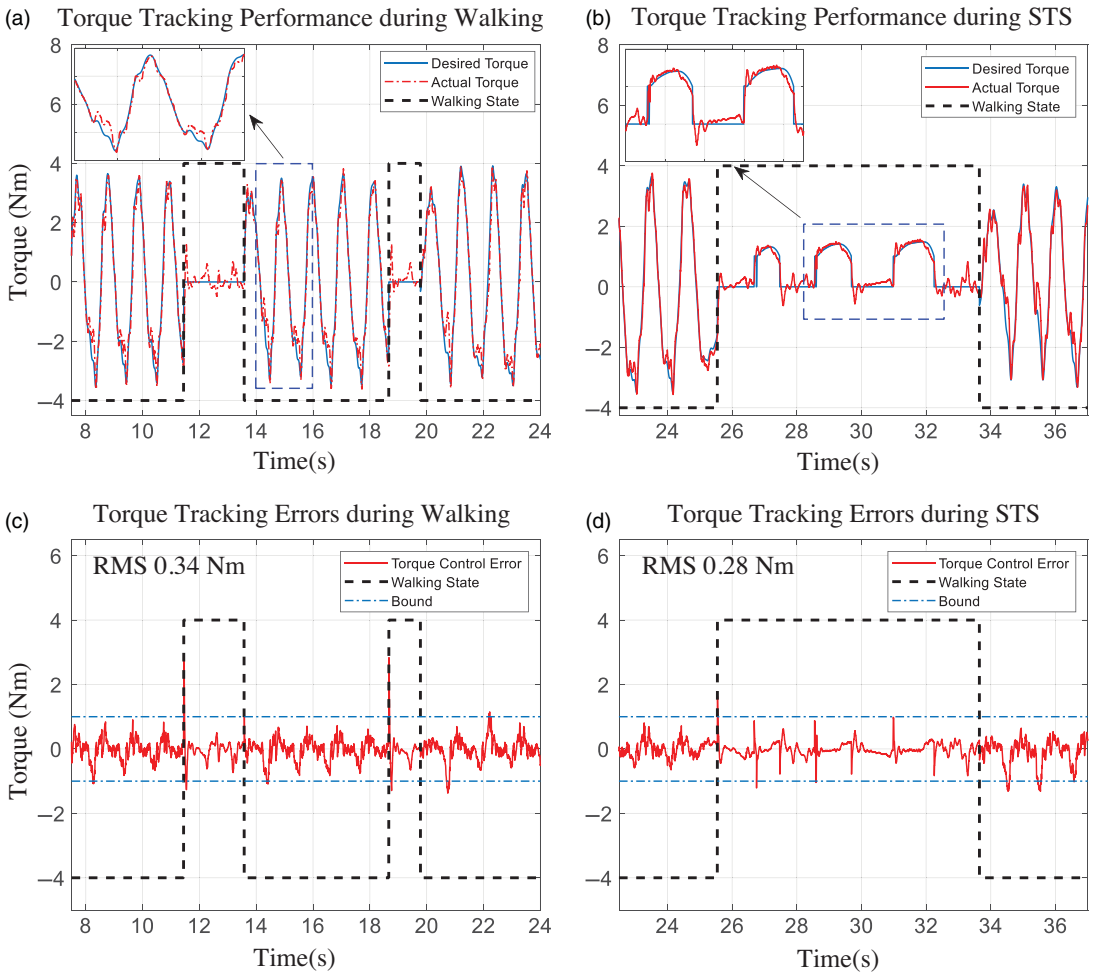


Fig. 12. Torque Tracking Performance in Hip Assistance Exoskeleton.

https://doi.org/10.1017/S0263574720000375 Published online by Cambridge University Press

Table III. Spatiotemporal parameters of human gait in each case

	Cases (Km/h)	MHR (deg)	Cadence (step/min)
Exo_A	2	35.48±4.41	38.71±2.54
	3	38.94±2.36	46.39±3.06
	4	43.72±3.19	51.83±1.34
NExo	2	28.95±2.37	43.38±7.90
	3	33.17±1.02	48.90±5.47
	4	38.42±0.74	55.08±3.76
Changes by assistance	2	22.55%	−10.77%
	3	17.38%	−5.12%
	4	13.79%	−5.90%

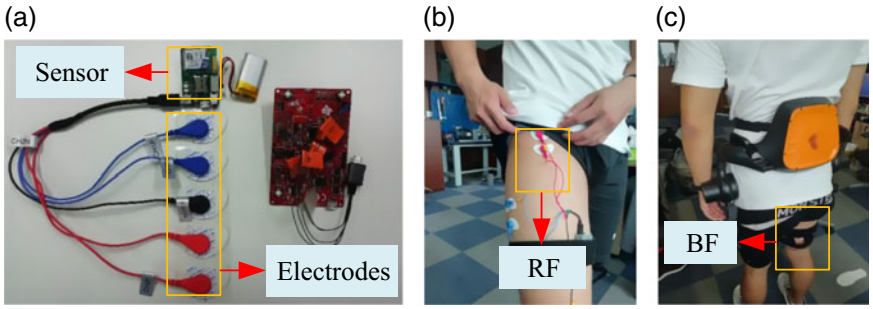


Fig. 13. Wireless sEMG sensors and recording positions. (a) Wireless sEMG system. (b) RF electrode. (c) BF electrode.

especially for the delayed input. Note that there still exist some errors left in physical exoskeleton experiments due to the discrete sampling data and uncertainties of modeling. Therefore, it is recommended to adopt a high sampling rate and a relatively accurate model when implementing this algorithm.

5.4. Assistance evaluation

Six healthy human subjects with an average age of 31±5 years, body weight of 73±8 Kg, height of 170±6 cm were recruited to evaluate the assistance effects. Each subject was asked to walk on the treadmill with speed 2, 3, 4 Km/h, and upstair activity respectively under NExo, Exo_A, and Exo_Z conditions, where NExo is walking without exoskeleton, and Exo_Z is walking with exoskeleton in zero torque mode, while Exo-A presents walking with FHAE in assistance mode. The exoskeleton hip joint trajectories and assistance torque were recorded with built-in encoders and torque sensors. Besides, two EMG electrodes were placed on the rectus femoris (RF) and biceps femoris (BF) as shown in Fig. 13 to record the muscle activities during walking and upstair activity. To be more convincing, each trial was repeated three times and all the joint kinematic and kinetic results are represented with an average value. The assistance performance is evaluated by the spatiotemporal parameter changes and muscle effort reduction rate in this article, which reflects the assistance effects on the external gait features and internal muscle voluntary force.

(1) Spatiotemporal Parameters

The hip trajectories of six subjects under 2, 3, and 4 Km/h treadmill walking are presented in Fig. 14, where the experimental gait trajectories are segmented into several complete gait cycles using phase synchronization algorithm. The maximum hip rotation range (MHR) in each case is also plotted with a histogram in Fig. 14. The cadence and step length parameters are compared to demonstrate the impacts of gait assistance. The cadence is estimated with the mounted IMU, and the step length is replaced with the MHR, which can be easily obtained from the exoskeleton system itself.

https://doi.org/10.1017/S0263574720000375 Published online by Cambridge University Press

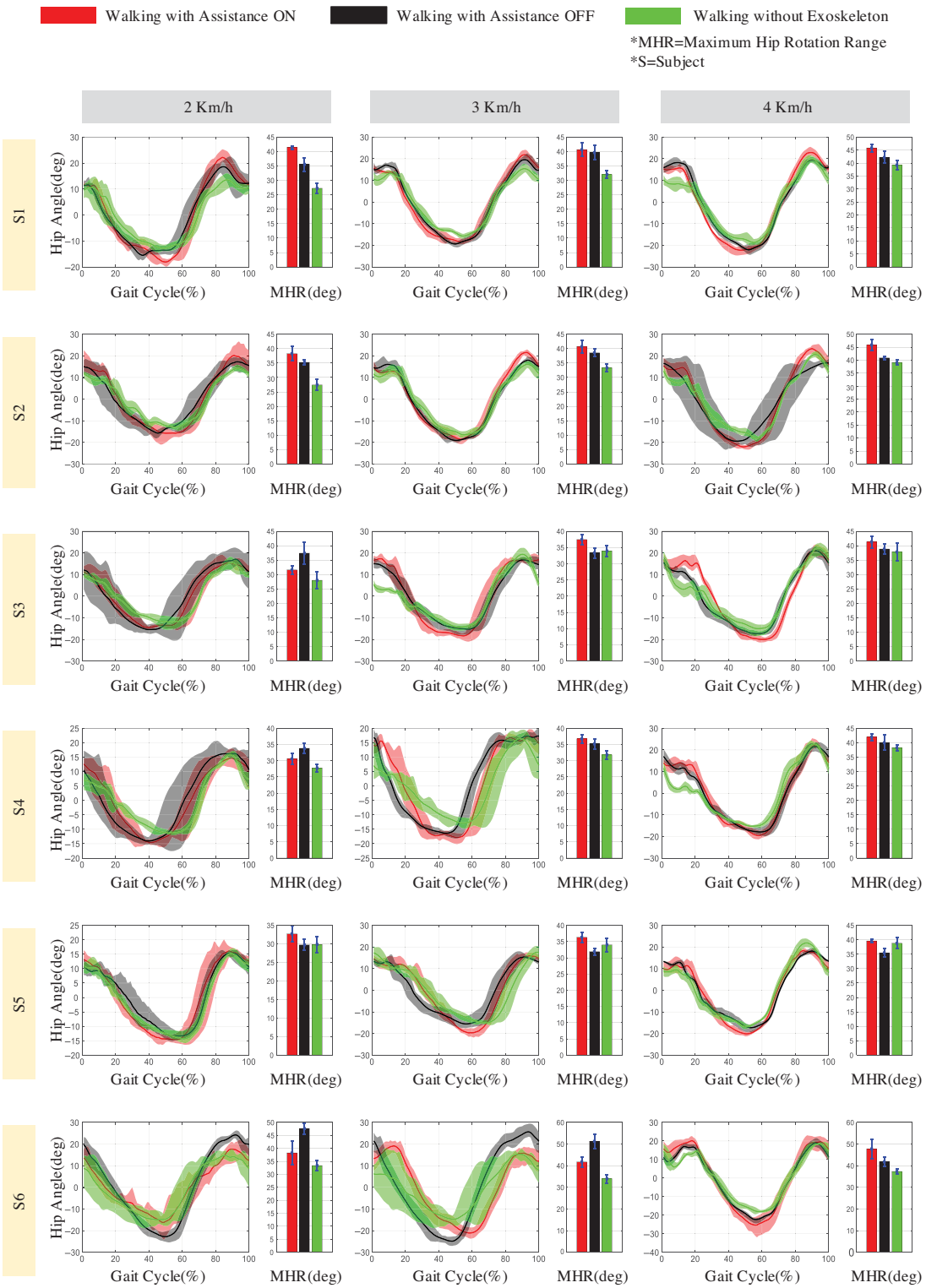


Fig. 14. Hip trajectories and maximum hip rotation range under three cases.

From Fig. 14, it can be obtained that there are no significant changes on the trajectory pattern except for the amplitude in all cases, which implies that the robotic exoskeleton is compliant and unlimited to the human. From the histogram, the MHR is obviously increased with the exoskeleton assistance, which results in decreased cadence at the same walking speed. Note that the results of Exo_Z are not so consistent, where both the increased and decreased MHR exist. In Exo_Z case, the

https://doi.org/10.1017/S0263574720000375 Published online by Cambridge University Press

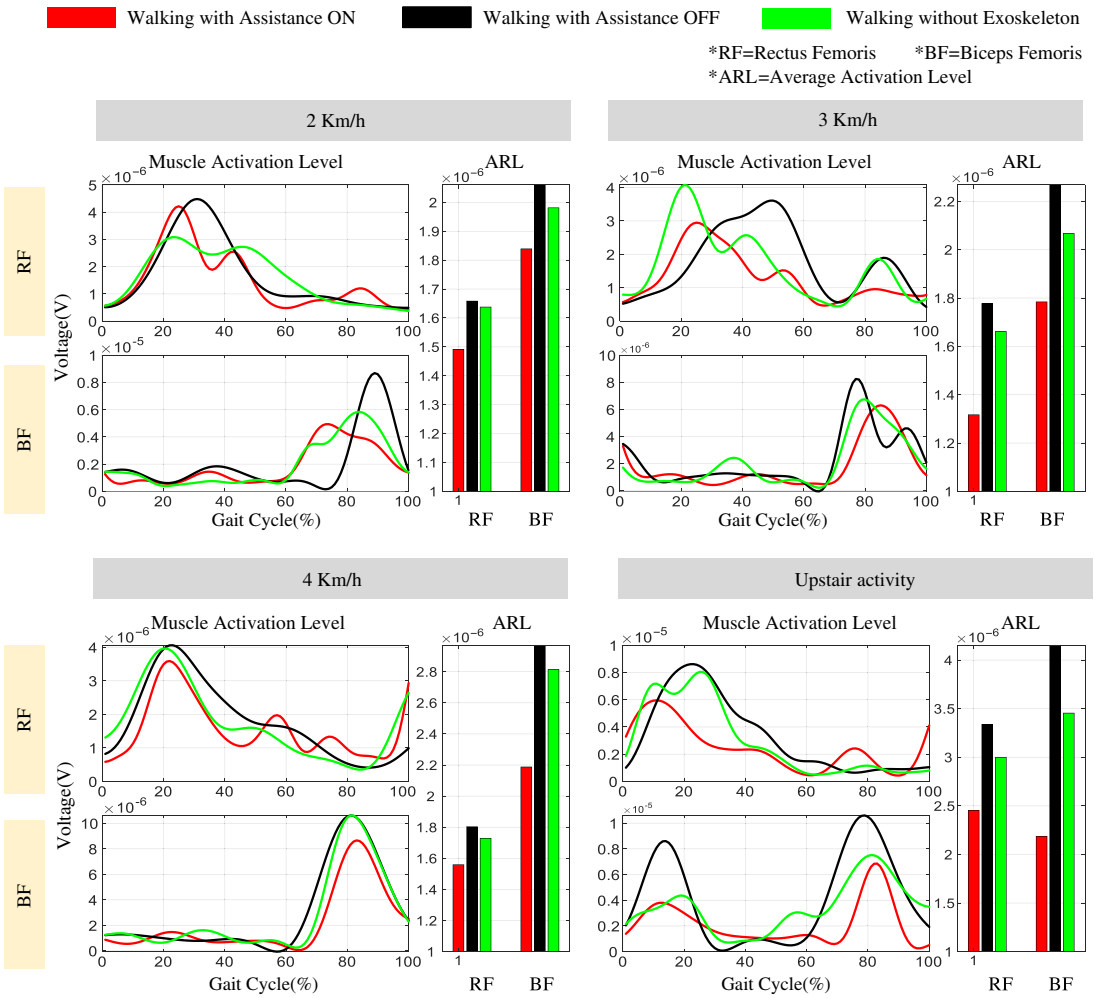


Fig. 15. Muscle activation levels during treadmill walking and upstair activity.

exoskeleton is purely an external load to the wearer, which might result in a diverse body response of human bodies. The average quantitative results of six subjects are shown in Table III.

(2) Muscle Effort Reduction with FHAE

In this part, the sEMG signals of 2, 3, 4 Km/h, and upstair activities under Exo_A, Exo_Z, and Nexo are presented to further demonstrate the assistance effects on the related muscle efforts. The biological sEMG signals are sampled with 1 Khz rate using a wireless collection system, and the raw data are filtered with four-order Butterworth high-pass filter to remove the movement artifacts, where the cutoff frequency is set 5 Hz. The moving average of the rectified sEMG signal is adopted as the activation level of skeletal muscle, which is calculated as

$$\alpha = 1/N \sum_{i=1}^{N} |x_i|,\ N = 50 \tag{60}$$

The results from an average gait cycle are shown in Fig. 15 and Table IV. The exoskeleton working in NExo is purely an external load to the wearers, thus as expected, the RF and BF muscle efforts are increased in NExo under all cases from the activation curves and bars. The muscle activation level curves in Exo_A is below the NExo case in most time, and the average muscle level bar graph also validates the decreased muscle effort with the exoskeleton assistance. Moreover, the reduction is more significant in strenuous activities, like 4 Km/h and upstair activity. It can be concluded that the assistance from exoskeleton not only compensates the exoskeleton load itself but also decreases the muscle efforts.

https://doi.org/10.1017/S0263574720000375 Published online by Cambridge University Press

Table IV. Muscle activation levels during walking and upstair activity

Cases	Muscle	Exo_A Unit:10^{-6} V	Exo_Z Unit:10^{-6} V	NExo Unit:10^{-6} V	Effort reduction (%)
2 Km/h	RF	1.49	1.66	1.64	9.15
	BF	1.84	2.06	1.98	7.07
3 Km/h	RF	1.32	1.78	1.66	20.48
	BF	1.78	2.27	2.07	14.01
4 Km/h	RF	1.56	1.80	1.73	9.83
	BF	2.19	2.97	2.81	22.06
Upstair activity	RF	2.45	3.34	3.00	18.33
	BF	2.19	4.15	3.45	36.52

The quantitative comparison results are shown in Table IV, and it can be obtained that both the RF and BF effort reductions are the lowest with 9.15% and 7.07% in 2 Km/h walking. In low-speed 2 Km/h walking, the step length and step frequency are small but the muscle effort is almost the same with 3 Km/h walking, and the slow motion limit the assistance amplitude, which results in lower effort reduction. In 3 Km/h and 4 Km/h experiments, which is closer to the speed of normal walking, the decreased RF and BF efforts validate the effectiveness of muscle effort reduction with the assistance of exoskeleton. Moreover, the human is most assisted in upstair activity, where the RF and BF reduction is up to 18.33% and 36.52%.

In all, the results of assistance evaluation experiments provide strong evidence to demonstrate the effectiveness of walking and upstair activity assistance with the hip exoskeletons. The gait pattern is obviously improved with increased gait length and decreased cadence. Moreover, the activation levels of hip-related muscles are significantly reduced, which implies that the human voluntary hip torque is also decreased. The above evidence shows great potential for improving walking efficiency and reducing metabolic energy consumption with the assistance torque.

6. Conclusion

This paper investigated the high-performance torque control algorithm for SEA forced controlled exoskeleton system, which is disturbed by ever-changing human–exoskeleton interaction, model uncertainties, and delayed input. The delay input caused by gait sensing is rarely considered but will degrade control performance and even cause instability. We proposed a novel FDOB to realize much better disturbance estimation performance than LDOB. Based on the disturbance sensing, a continuous fractional power control law is designed to achieve perfect matched/unmatched disturbance rejection and finite-time convergence. Finally, the proposed CFTC control scheme has been successfully implemented into the simulation, physical SEA testing platform, and all the results demonstrated the unique properties of proposed CFTC, that is, high accuracy, fast convergence rate, perfect disturbance rejection capability, well static–dynamic performance, and strong robustness. Furthermore, the assistance effects are evaluated with six human subjects, and the results present improved gait pattern, reduced muscle activations, and consequently decreased muscle efforts with the exoskeleton assistance.

Acknowledgments

This research is supported by Move Robotics Technology Company, Ltd. and the National Nature Science Foundation of China (No. 51705136).

References

1. T. Xue, Z. Wang, T. Zhang and M. Zhang, "Adaptive oscillator-based robust control for flexible hip assistive exoskeleton," *IEEE Robot. Autom. Lett.* **4**(4), 3318–3323 (2019).
2. J. Meuleman, E. van Asseldonk, G. van Oort, H. Rietman and H. van der Kooij, "LOPES II—Design and evaluation of an admittance controlled gait training robot With shadow-leg approach," *IEEE Trans. Neural Syst. Rehabil. Eng.* **24**(3), 352–363 (2016).

https://doi.org/10.1017/S0263574720000375 Published online by Cambridge University Press

3. H. J. Lee, S. Lee, W. H. Chang, K. Seo, Y. Shim, B. O. Choi, G. H. Ryu and Y. H. Kim, "A wearable hip assist robot can improve gait function and cardiopulmonary metabolic efficiency in elderly adults," *IEEE Trans. Neural Syst. Rehabil. Eng.* **25**(9), 1549–1557 (2017).
4. T. Xue, Z. Wang, T. Zhang, M. Zhang and Z. Li, "The Control System for Flexible Hip Assistive Exoskeleton," *Proceedings of 2018 IEEE International Conference on Robotics and Biomimetics (ROBIO)* (2018) pp. 697–702.
5. Y. Shuanghe, Y. Xinghuo and R. J. Stonier, "Continuous finite-time control for robotic manipulators with terminal sliding mode," *Automatica* **41**(11), 1957–1964 (2005).
6. Z. Wang, T. Xue, B. Liang, and Z. Chen, "Backstepping Based Robust Control for Space Tele-Robot Systems with Finite-Time Convergence," *Proceedings of 2018 IEEE International Conference on Robotics and Biomimetics (ROBIO)* (2018) pp. 1419–1424.
7. X. Bing and S. Yin, "Velocity-free fault-tolerant and uncertainty attenuation control for a class of nonlinear systems," *IEEE Trans. Ind. Electron.* **63**(7), 4400–4411 (2016).
8. Y. Shtessel, C. Edwards, L. Fridman and A. Levant, *Sliding Mode Control and Observation* (Springer, New York, 2014).
9. L. Shihua, S. Haibin, J. Yang and Y. Xinghuo, "Continuous finite-time output regulation for disturbed systems under mismatching condition," *IEEE Trans. Autom. Control* **60**(1), 277–282 (2015).
10. L. Shihua, D. Shihong and L. Qi, "Global set stabilisation of the spacecraft attitude using finite-time control technique," *Int. J. Control* **82**(5), 822–836 (2009).
11. W. Meng, S. Lei, W. Yin, D. Shuai and L. Jingtai, "Continuous Finite-Time Control Approach for Series Elastic Actuator," *Proceedings of IEEE Conference on Decision and Control* (2016) pp. 843–848.
12. G. Pratt and M. Williamson, "Human Robot Interaction and Cooperative Robots," *Proceedings of IEEE/RSJ International Conference on Intelligent Robots and Systems* (1995) pp. 399–406.
13. S. Keehong, K. R. Kyung and J. P. Young, "Adaptive Oscillator-Based Control for Active Lower-Limb Exoskeleton and its Metabolic Impact," *Proceedings of IEEE International Conference on Robotics and Automation* (2018) pp. 6752–6758.
14. Y. Lee, Y. J. Kim, J. Lee, M. Lee, B. Choi, J. Kim, Y. J. Park and J. Choi, "Biomechanical design of a novel flexible exoskeleton for lower extremities," *IEEE/ASME Trans. Mechatron.* **22**(5), 2058–2069 (2017).
15. W. Huo, S. Mohammed, Y. Amirat and K. Kong, "Fast gait mode detection and assistive torque control of an exoskeletal robotic orthosis for walking assistance," *IEEE Trans. Robot.* **34**(4), 1035–1052 (2018).
16. A. Calanca and F. Paolo, "Human-adaptive control of series elastic actuators," *Robotica* **32**(8), 1301–1316 (2014).
17. A. Calanca, C. Luca and F. Paolo, "Robust force control of series elastic actuators," *Actuators* **3**(3), 182–204 (2014).
18. K. Kyoungchul, B. Joonbum and T. Masayoshi, "Control of rotary series elastic actuator for ideal force-mode actuation in human–robot interaction applications," *IEEE/ASME Trans. Mechatron.* **14**(1), 105–118 (2009).
19. M. Matsuda, Y. Mataki, H. Mutsuzaki, K. Yoshikawa, K. Takahashi, K. Enomoto, K. Sano, M. Mizukami, K. Tomita, H. Ohguro and N. Iwasaki, "Immediate effects of a single session of robot-assisted gait training using Hybrid Assistive Limb (HAL) for cerebral palsy," *J. Phys. Ther. Sci.* **30**(2), 207–212 (2018).
20. S. R. Soekadar, W. Matthias and G. P. Cristina, "Hybrid EEG/EOG-based brain/neural hand exoskeleton restores fully independent daily living activities after quadriplegia." *Sci. Robot.* **1**(1), eaag3296-1 (2016).
21. E. Zheng, S. Manca, T. Yan, A. Parri, N. Vitiello and Q. Wang, "Gait phase estimation based on noncontact capacitive sensing and adaptive oscillators," *IEEE Trans. Biomed. Eng.* **64**(10), 2419–2430 (2017).
22. W. Qingcong, W. Xingsong, D. Fengpo and Z. Xiaobo, "Design and control of a powered hip exoskeleton for walking assistance," *Int. J. Adv. Robot. Syst.* **12**(3), 18 (2015).
23. C. L. Vaughan, B. L. Davis and J. C. O'connor, *Dynamics of Human Gait* (Kiboho Publishers, Cape Town, 1999).
24. E. F. Beckenbach and R. Bellman, *Inequalities*, vol. 30 (Springer Science & Business Media, Berlin, Germany, 2012).
25. D. Shihong and L. Shihua, "Second-order sliding mode controller design subject to mismatched term," *Automatica* **77**, 388–392 (2017).
26. T. M. Manini, S. L. Hong and C. C. Brian, "Aging and muscle: A neuron's perspective," *Curr. Opin. Clin. Nutr. Metab. Care* **16**(1), 21–26 (2013).
27. J. Sungho, "Hypothetical neural control of human bipedal walking with voluntary modulation," *Med. Biolog. Eng. Comput.* **46**(2), 179–193 (2008).
28. Z. Jamaludin, V. B. Hendrik and S. Jan, "Friction compensation of an XY feed table using friction-model-based feedforward and an inverse-model-based disturbance observer," *IEEE Trans. Ind. Electron.* **56**(10), 3848–3853 (2009).
29. C. Wenhua, D. J. Ballance and P. J. Gawthrop, "A nonlinear disturbance observer for robotic manipulators," *IEEE Trans. Ind. Electron.* **47**(4), 932–938 (2000).
30. T. Zhang, M. Tran and H. Huang, "Admittance shaping-based assistive control of SEA-driven robotic hip exoskeleton," *IEEE/ASME Trans. Mechatron.* **24**(4), 1508–1519 (2019).
31. G. Aguirre-Ollinger, A. Narayan, H. J. Cheng and H. Yu, "Exoskeleton Control for Post-stoke Gait Training of a Paretic Limb Based on Extraction of the Contralateral Gait Phase," *Proceedings of International Symposium on Wearable Robotics* (2018) pp. 294–298.

https://doi.org/10.1017/S0263574720000375 Published online by Cambridge University Press

32. S. Keehong, L. Jusuk, L. Younbaek and H. Taesin, "Fully Autonomous Hip Exoskeleton Saves Metabolic Cost of Walking." *Proceedings of 2016 IEEE International Conference on Robotics and Automation* (2016) pp. 4628–4635.
33. W. Ziwei, C. Zhang, Z. Yiman and Y. Xingyao, "Adaptive finitetime control for bilateral teleoperation systems with jittering time delays." *Int. J. Robust Nonlinear Control* **29**(4), 1007–1030 (2018).
34. K. Kammen, A. M. Boonstra, L. H. V. Woude, H. A. Reinders-Messelink and R. Otter, "The combined effects of guidance force, bodyweight support and gait speed on muscle activity during able-bodied walking in the Lokomat," *Clin. Biomechan.* **36**, 65–73 (2016).
35. A. Jayaraman, M. K. O'brien, S. Madhavan, C. K. Mummidisetty, H. R. Roth, K. Hohl, A. Tapp, K. Brennan, M. Kocherginsky, K. J. Williams, H. Takahashi and W. Z. Rymer, "Stride management assist exoskeleton vs functional gait training in stroke: A randomized trial," *Neurology* **92**(3), 263–273 (2019).
36. S. Oh and K. Kong, "High-precision robust force control of a series elastic actuator," *IEEE/ASME Trans. Mechatron.* **22**(1), 71–80 (2016).
37. N. Paine, S. Oh and L. Sentis, "Design and control considerations for high-performance series elastic actuators," *IEEE/ASME Trans. Mechatron.* **19**(3), 1080–1091 (2013).
38. Y. Park, N. Paine and S. Oh, "Development of force observer in series elastic actuator for dynamic control," *IEEE Trans. Ind. Electron.* **65**(3), 2398–2407 (2017).
39. X. Li, Y. H. Liu and H. Yu, "Iterative learning impedance control for rehabilitation robots driven by series elastic actuators," *Automatica* **90**, 1–7 (2018).
40. J. C. Pérez-Ibarra, A. L. J. Alarcón, J. C. Jaimes, F. M. E. Ortega, M. H. Terra and A. A. G. Siqueira, "Design and Analysis of $\mathbf{H}\infty$ Force Control of a Series Elastic Actuator for Impedance Control of an Ankle Rehabilitation Robotic Platform," *Proceedings of 2017 American Control Conference (ACC)* (2017) pp. 2423–2428.
41. A. Calanca and P. Fiorini, "Impedance control of series elastic actuators based on well-defined force dynamics," *Robot. Auto. Syst.* **96**, 81–92 (2017).
42. G. Aguirre-Ollinger, "Exoskeleton control for lower-extremity assistance based on adaptive frequency oscillators: Adaptation of muscle activation and movement frequency," *J. Eng. Med.* **229**(1), 52–68 (2015).
43. T. Yan, A. Parri, V. R. Garate, M. Cempini, R. Ronsse and N. Vitiello, "An oscillator-based smooth real-time estimate of gait phase for wearable robotics," *Auto. Robots* **41**(3), 759–774 (2017).
44. J. Kim, G. Lee, R. Heimgartner, D. A. Revi, N. Karavas, D. Nathanson, I. Galiana, A. Eckert-Erdheim, P. Murphy, D. Perry, N. Menard, D. K. Choe, P. Malcolm and C. J. Walsh, "Reducing the metabolic rate of walking and running with a versatile, portable exosuit," *Science* **365**(6454), 668–672 (2019).

https://doi.org/10.1017/S0263574720000375 Published online by Cambridge University Press